The EDGE-CALIFA Survey: Molecular and Ionized Gas Kinematics in Nearby Galaxies

Rebecca C. Levy[1] , Alberto D. Bolatto[1] , Peter Teuben[1] , Sebastián F. Sánchez[2] , Jorge K. Barrera-Ballesteros[3] ,
Leo Blitz[4] , Dario Colombo[5], Rubén García-Benito[6] , Rodrigo Herrera-Camus[7] , Bernd Husemann[8] , Veselina Kalinova[5],
Tian Lan[9,10], Gigi Y. C. Leung[8] , Damián Mast[11,12] , Dyas Utomo[4,13] , Glenn van de Ven[8,14] , Stuart N. Vogel[1], and
Tony Wong[9]

[1] Department of Astronomy, University of Maryland, College Park, MD 20742, USA; rlevy@astro.umd.edu
[2] Instituto de Astronomía, Universidad Nacional Autónoma de México, A.P. 70-264, 04510 México, D.F., Mexico
[3] Department of Physics & Astronomy, Johns Hopkins University, Baltimore, MD 21218, USA
[4] Department of Astronomy, University of California, Berkeley, CA 94720, USA
[5] Max-Planck-Institut für Radioastronomie, D-53121, Bonn, Germany
[6] Instituto de Astrofísica de Andalucía, CSIC, E-18008 Granada, Spain
[7] Max-Planck-Institut für Extraterrestrische Physik, D-85741 Garching bei Müchan, Germany
[8] Max-Planck-Institut für Astronomie, Königstuhl 17, D-69117 Heidelberg, Germany
[9] Department of Astronomy, University of Illinois, Urbana, IL 61801, USA
[10] Department of Astronomy, Columbia University, New York, NY 10027, USA
[11] Universidad Nacional de Córdoba, Observatorio Astronómico de Córdoba, Córdoba, Argentina
[12] Consejo de Investigaciones Científicas y Técnicas de la República Argentina, C1033AAJ, CABA, Argentina
[13] Department of Astronomy, The Ohio State University, Columbus, OH 43210, USA
[14] European Southern Observatory (ESO), D-85748 Garching bei München, Germany
Received 2018 January 23; revised 2018 May 2; accepted 2018 May 3; published 2018 June 15

Abstract

We present a comparative study of molecular and ionized gas kinematics in nearby galaxies. These results are based on observations from the EDGE survey, which measured spatially resolved $^{12}CO(J = 1$–$0)$ in 126 nearby galaxies. Every galaxy in EDGE has corresponding resolved ionized gas measurements from CALIFA. Using a sub-sample of 17 rotation-dominated, star-forming galaxies where precise molecular gas rotation curves could be extracted, we derive CO and Hα rotation curves using the same geometric parameters out to $\gtrsim 1$ R_e. We find that $\sim$75% of our sample galaxies have smaller ionized gas rotation velocities than the molecular gas in the outer part of the rotation curve. In no case is the molecular gas rotation velocity measurably lower than that of the ionized gas. We suggest that the lower ionized gas rotation velocity can be attributed to a significant contribution from extraplanar diffuse ionized gas in a thick, turbulence-supported disk. Using observations of the Hγ transition, also available from CALIFA, we measure ionized gas velocity dispersions and find that these galaxies have sufficiently large velocity dispersions to support a thick ionized gas disk. Kinematic simulations show that a thick disk with a vertical rotation velocity gradient can reproduce the observed differences between the CO and Hα rotation velocities. Observed line ratios tracing diffuse ionized gas are elevated compared to typical values in the midplane of the Milky Way. In galaxies affected by this phenomenon, dynamical masses measured using ionized gas rotation curves will be systematically underestimated.

Key words: galaxies: ISM – galaxies: kinematics and dynamics – ISM: kinematics and dynamics – ISM: molecules

1. Introduction

Studying the molecular and ionized gas components of a galaxy gives powerful insights into various stages of star formation. The gas kinematics can reveal feedback mechanisms, such as inflows and outflows, and merger events that alter the star formation history (SFH) of the galaxy. The measurement of molecular kinematics of galaxies, as traced by ^{12}CO, has vastly improved in recent years due to the advent of interferometers that allow for measurements at high spatial and spectral resolutions. Similar advances have been made in the optical regime, through the use of integral field units (IFUs). Studying the multiwavelength kinematic properties of nearby galaxies provides information about their formation, SFH, and evolution.

The multiwavelength kinematics of disk galaxies have been compared in a number of case studies. Wong et al. (2004), Yim et al. (2014), and Frank et al. (2016) compare H I and CO kinematics and generally find good agreement between the rotation velocities of the atomic and molecular components. However, comparisons with the ionized gas often lead to

different results. Most notable is NGC 891, which shows vertical gradients in the rotation velocity ("lags") in H I of -10 to -20 km s^{-1} kpc^{-1} (Swaters et al. 1997; Fraternali et al. 2005) and in ionized gas of -15 km s^{-1} kpc^{-1} (Heald et al. 2006a). Similar lags in Hα and H I are seen in NGC 5775 (Lee et al. 2001), where the CO and Hα rotation velocities agree in the midplane (Heald et al. 2006b). However, lags between the H I and Hα do not always agree (Fraternali et al. 2004, 2005; Zschaechner et al. 2015; Zschaechner & Rand 2015). de Blok et al. (2016) study the CO, H I, and [C II] kinematics in ten nearby galaxies and find that the [C II] velocity is systematically larger than that of the CO or H I, although they attribute this to systematics in the data reduction and the low-velocity resolution of the [C II] data. Simon et al. (2005) compare CO and Hα rotation curves in two disk galaxies: in NGC 5963, the CO and Hα velocities agree to within 1 km s^{-1}; the Hα in NGC 4605, however, shows systematically slower rotation than the CO, by 4.8 km s^{-1}. Clearly, comparisons among tracers of the different phases of the interstellar medium (ISM) are complicated. Large, homogeneous samples of galaxies in multiple tracers are needed to

make headway toward understanding the causes and ubiquity of the kinematic differences between ISM phases.

Davis et al. (2013) studied the properties of 24 gas-rich early-type galaxies from the ATLAS^{3D} survey by comparing the ionized, atomic, and molecular gas kinematics out to $\sim$0.5 R_e. They find that 80% of their sample show faster molecular gas rotation velocities than the ionized gas. The other 20% have the same molecular and ionized gas rotation velocities. They attribute these rotation velocity differences to the velocity dispersion of the ionized gas. Therefore, the dynamically cold molecular gas is a better tracer of the circular velocity than the ionized gas. Such a study has yet to be carried out in a similar sample of star-forming disk galaxies.

One way to study the kinematics of a galaxy is through its rotation curve, i.e., the rotation velocity as a function of galactocentric radius. The velocity can be decomposed into rotational, radial, and higher-order terms (e.g., Begeman 1989; Schoenmakers 1999; van de Ven & Fathi 2010). High spatial resolution data are needed to construct robust rotation curves using this method. There has been a dearth of such high-resolution data on a large sample of galaxies, particularly for the molecular gas tracers. The CALIFA IFU survey (Sánchez et al. 2012) measured optical spectra of 667 nearby galaxies, providing spatially and spectrally resolved Hα velocities, as well as intensities, velocities, and velocity dispersions for many other ionized gas lines. The EDGE-CALIFA survey (EDGE, Bolatto et al. 2017), selected 126 galaxies from CALIFA and observed them in ^{12}CO($J = 1 - 0$) with the Combined Array for Millimeter Wave Astronomy (CARMA) at $\sim$4.''5 resolution. Together, these surveys allow for the molecular and ionized gas kinematics of a statistical sample of nearby, star-forming galaxies to be analyzed. Using a sub-sample of 17 EDGE-CALIFA galaxies, this work constitutes the largest spatially resolved combined CO and Hα kinematic analysis to date for late-type galaxies.

Section 2 presents the EDGE, CALIFA, and ancillary data used for this study. The rotation curve fitting routine, procedure to determine the kinematic parameters from the EDGE CO data, and the sub-sample of galaxies used in this work are discussed in Section 3. Section 4 presents comparisons of the CO and Hα rotation curves. Potential explanations and interpretations of the results are presented in Section 5, including the results of the kinematic simulations, velocity dispersions, and ionized gas line ratios. We present our conclusions and summary in Section 6. Throughout this paper, CO refers to ^{12}C^{16}O($J = 1 - 0$).

2. Observations and Data Reduction

2.1. The EDGE-CALIFA Survey

The EDGE-CALIFA survey (Bolatto et al. 2017) measured CO in 126 nearby galaxies with CARMA in the D and E configurations. Full details of the survey, data reduction, and masking techniques are discussed in Bolatto et al. (2017), but we present a brief overview here. The EDGE galaxies were selected from the CALIFA sample (discussed in the following section) based on their infrared (IR) brightness and are biased toward higher star formation rates (SFRs) (see Figure 6 of Bolatto et al. 2017). A pilot study of 177 galaxies was observed with the CARMA E-array. From this sample, 126 galaxies selected for CO brightness were re-observed in the D-array. These 126 galaxies with combined D and E array data

constitute the main EDGE sample.[15] The EDGE sample is the largest sample of galaxies with spatially resolved CO, at a typical angular resolution of 4.''5 (corresponding to $\sim$1.5 kpc at the mean distance of the sample). Data cubes were produced with 20 km s^{-1} velocity channels. At each pixel in the cube, a Gaussian is fit to the CO line. Velocity-integrated intensity, mean velocity, velocity dispersion, and associated error maps are created from the Gaussian fits. Pixels with velocities that differ from their nearest (non-blanked) neighbors by more than 40 km s^{-1}, generally caused by fitting failures in low signal-to-noise data, are replaced with the median value of the neighbors. This replacement is rare, occurring for only $\sim$0.5% of pixels in a given galaxy. Additional masking was applied to the CO maps where the Gaussian fitting introduced artifacts. This masking was based on a signal-to-noise ratio (S/N) cut using the integrated intensity and associated error map. Pixels with S/N $<$ 1 were blanked in the velocity field. Average CO velocity dispersions are derived and are listed in Table 1. A beam smearing correction is applied and is discussed in Appendix B.

2.2. The CALIFA Survey

The CALIFA survey (Sánchez et al. 2012) observed 667 nearby ($z = 0.005$–0.03) galaxies. Full details of the CALIFA observations are presented in Walcher et al. (2014) and other CALIFA papers, but we present a brief overview for completeness. CALIFA used the PPAK IFU on the 3.5 m Calar Alto observatory with two spectral gratings. The low-resolution grating (V500) covered wavelengths from 3745 to 7500 Å with 6.0 Å (FWHM) spectral resolution, corresponding to an FWHM velocity resolution of 275 km s^{-1} at Hα. The moderate-resolution grating (V1200) covered wavelengths from 3650 to 4840 Å with 2.3 Å (FWHM) spectral resolution, corresponding to an FWHM velocity resolution of 160 km s^{-1} at Hγ (Sánchez et al. 2016a). The V500 grating includes many bright emission lines, including Hα, Hβ, Hγ, Hδ, the [N II] doublet, and the [S II] doublet. The V1200 grating contains many stellar absorption features used to derive the stellar kinematics as well as a few ionized gas emission lines, such as Hγ and Hδ. The typical spatial resolution of the CALIFA data are 2.''5, corresponding to $\sim$0.8 kpc at the mean distance of the galaxies. The CALIFA galaxies were selected from the Sloan Digital Sky Survey (SDSS) DR7 to have angular isophotal diameters between 45'' and 79.''2, in order to make the best use of the PPAK field of view. The upper redshift limit was set so that all targeted emission lines were observable for all galaxies in both spectral setups; the lower redshift limit was set so that the sample would not be dominated by dwarf galaxies. The data used for this study come from the final data release[16] (Sánchez et al. 2016a) and data products come from Pipe3D version 2.2 (Sánchez et al. 2016b, 2016c), provided in their final form by the CALIFA Collaboration.

The wavelength calibration of the data is detailed in Sánchez et al. (2012) and Appendix A.5 of Husemann et al. (2013) and is crucial to extract accurate line velocities. The wavelength calibration data are used to resample the spectra to a linear wavelength grid and to homogenize the spectral resolution

---

[15] The EDGE CO data cubes and moment maps for the main sample are publicly available and can be downloaded from http://www.astro.umd.edu/EDGE.

[16] The CALIFA data cubes are publicly available at http://califa.caha.es.

Table 1
Parameters for the KSS

Name	Morph (Type)	log(M_*) ($M_\odot$)	log(SFR) ($M_\odot$ yr^{-1})	d (Mpc)	D_{25} (′)	CO V_{max} (km s^{-1})	ΔV (km s^{-1})	H I W50 (km s^{-1})	H I W90 (km s^{-1})	Σ_* ($M_\odot$ pc^{-2})	σ_{CO} (km s^{-1})	σ_{ADC} (km s^{-1})	$\sigma_{H\gamma}$ (km s^{-1})	[S II]/Hα	[N II]/Hα
IC1199	Sbc (3.7)	10.8	0.2	68.3	1.2	199.0 ± 5.7	2.6 ± 4.3	141.8	229.0	189.6	11.1 ± 5.5	52.1 ± 26.5	34.6 ± 9.2	0.19 ± 0.01	0.39 ± 0.01
NGC2253	Sc (5.8)	10.8	0.5	51.2	1.4	174.2 ± 7.9	1.1 ± 7.7	211.0	243.9	205.6	9.2 ± 2.5	24.9 ± 37.2	28.0 ± 3.4	0.17 ± 0.01	0.37 ± 0.01
NGC2347	Sb (3.1)	11.0	0.5	63.7	1.6	285.6 ± 2.0	24.1 ± 0.4	267.7	289.2	336.5	10.1 ± 4.0	85.9 ± 5.0	36.6 ± 5.1	0.18 ± 0.01	0.38 ± 0.01
NGC2410	Sb (3.0)	11.0	0.5	67.5	2.2	227.2 ± 5.9	15.3 ± 5.1	247.3	267.3	198.6	17.6 ± 7.5	67.7 ± 16.5	38.2 ± 12.1	0.20 ± 0.01	0.47 ± 0.04
NGC3815	Sab (2.0)	10.5	0.0	53.6	1.4	185.8 ± 5.2	18.8 ± 3.6	176.5	223.5	215.4	15.1 ± 5.1	52.9 ± 8.0	26.9 ± 3.3	0.20 ± 0.02	0.38 ± 0.01
NGC4047	Sb (3.2)	10.9	0.6	49.1	1.5	216.3 ± 2.2	14.3 ± 0.5	220.3	243.2	296.6	9.5 ± 2.4	63.2 ± 9.5	29.5 ± 3.7	0.16 ± 0.01	0.35 ± 0.01
NGC4644	Sb (3.1)	10.7	0.1	71.6	1.5	186.1 ± 5.8	13.5 ± 2.8	171.0	214.7	132.6	16.6 ± 8.1	53.2 ± 10.9	31.3 ± 7.7	0.16 ± 0.01	0.40 ± 0.01
NGC4711	SBb (3.2)	10.6	0.1	58.8	1.2	142.8 ± 10.5	5.8 ± 0.9	167.3	185.2	121.1	10.0 ± 4.4	47.9 ± 37.2	32.9 ± 7.7	0.18 ± 0.01	0.36 ± 0.01
NGC5016	SABb (4.4)	10.5	−0.0	36.9	1.6	178.4 ± 0.8	17.7 ± 8.7	187.2	199.1	248.9	11.3 ± 5.6	56.4 ± 11.0	26.6 ± 3.8	0.16 ± 0.01	0.38 ± 0.01
NGC5480	Sc (5.0)	10.2	0.2	27.0	1.7	111.4 ± 6.6	4.8 ± 5.1	147.7	⋯	180.0	11.2 ± 3.5	37.1 ± 41.5	24.0 ± 2.9	0.20 ± 0.01	0.33 ± 0.01
NGC5520	Sb (3.1)	10.1	−0.1	26.7	1.6	162.3 ± 0.2	15.3 ± 1.4	158.1	170.1	202.3	13.4 ± 6.8	60.5 ± 0.4	26.5 ± 2.5	0.20 ± 0.01	0.39 ± 0.01
NGC5633	Sb (3.2)	10.4	0.2	33.4	1.1	187.5 ± 9.4	9.1 ± 2.9	200.6	⋯	396.0	11.3 ± 2.5	53.3 ± 23.4	25.1 ± 1.8	0.17 ± 0.01	0.37 ± 0.01
NGC5980	Sbc (4.4)	10.8	0.7	59.4	1.6	216.3 ± 4.4	8.2 ± 4.8	219.4	248.6	214.8	12.3 ± 2.3	52.5 ± 24.0	34.3 ± 3.8	0.17 ± 0.01	0.41 ± 0.01
UGC04132	Sbc (4.0)	10.9	1.0	75.4	1.2	238.5 ± 11.4	16.3 ± 8.0	255.6	291.5	206.5	15.8 ± 3.9	79.4 ± 40.0	33.1 ± 4.3	0.20 ± 0.01	0.40 ± 0.01
UGC05111	Sbc (4.0)	10.8	0.6	98.2	1.5	216.2 ± 11.9	9.1 ± 4.4	⋯	⋯	154.4	15.4 ± 3.6	52.2 ± 33.5	⋯	0.23 ± 0.02	0.41 ± 0.02
UGC09067	Sab (2.0)	11.0	0.7	114.5	0.8	211.7 ± 4.2	1.0 ± 2.1	212.7	⋯	110.7	14.1 ± 7.6	12.5 ± 40.7	29.0 ± 4.9	0.21 ± 0.01	0.35 ± 0.01
UGC10384	Sab (1.6)	10.3	0.7	71.8	1.2	187.4 ± 8.1	14.2 ± 7.0	180.7	200.9	74.5	18.9 ± 6.2	45.0 ± 12.9	35.4 ± 2.7	0.21 ± 0.01	0.35 ± 0.02

Note. The table lists relevant parameters for the KSS galaxies not already listed in Table 3. The morphology and types are from HyperLeda and are listed in Bolatto et al. (2017). Values for M_*, SFR, distances (d), and the diameter of the 25th magnitude isophote (D_{25}) are taken from CALIFA and are also found in Bolatto et al. (2017). Errors on log(M_*) and log(SFR) are ±0.1 in the corresponding units. CO V_{max} is the maximum CO rotation velocity, determined by the median of the CO RC at radii larger than twice the CO beam; the error is the standard deviation. Here, ΔV is the median difference between CO and Hα RCs, as described in Section 4. H I W50 and W90 listed here are uncorrected for inclination. All values are taken from the GBT, except for NGC 5480, NGC 5633, and UGC 9067 (see Section 2.4). In this table, Σ_* are averages of stellar surface density radial profiles from (Utomo et al. 2017), σ_{CO} are the velocity dispersions estimated from the beam smearing corrected CO maps (Section 2.1), σ_{ADC} are the velocity dispersions estimated from the ADC (Section 5.5.2), and $\sigma_{H\gamma}$ are the median velocity dispersions measured from the Hγ line; errors are the weighted standard deviations (Section 5.5.1). [S II]/Hα and [N II]/Hα are median intensity ratios, where the error is the standard error described in Section 5.6.

across the band (6.0 Å FWHM for V500 and 2.3 Å FWHM for V1200). The calibration is done using HeHgCd lamp exposures before and after each pointing, using 16 lines for the V500 data and 11 lines for the V1200 data. The resulting accuracy of the wavelength calibration is ~0.2–0.3 Å for the V500 data and ~0.1–0.2 Å for the V1200 data. However, in our analysis of the V1200 data, we found errors in the wavelength calibration resulting from a bad line choice used to anchor the wavelength scale. This has been remedied in the current version of the data used here.

Once the data are calibrated, Pipe3D fits and removes the stellar continuum, measures emission line fluxes, and produces two-dimensional data products for each emission line. Full details of Pipe3D and its application to the CALIFA data can be found in Sánchez et al. (2016b, 2016c), and important details are reproduced here for completeness. The underlying stellar continuum is fit and subtracted to produce a continuum-subtracted or "emission line only" spectrum (Section 2 of Sánchez et al. 2016b). A Monte Carlo method is used to first determine the nonlinear stellar kinematic properties and dust attenuation at each pixel in the cube. Next, the results of this nonlinear fitting are fixed and the properties of the underlying stellar population are determined from a linear combination of simple stellar population (SSP) templates (see also Section 3.2 of Sánchez et al. 2016c). This model stellar spectrum is then subtracted from the CALIFA cube at each pixel to produce a continuum-subtracted cube. To determine the properties of the emission lines, Pipe3D uses a nonparametric fitting routine optimized for weaker emission lines ("flux_elines") that extracts only the line flux intensity, velocity, velocity dispersion, and equivalent width (EW) (see Section 3.6 of Sánchez et al. (2016c) for full details). Each emission line of interest is fit using a moment analysis similar to optimal extraction. The line centroid is first guessed based on the rest-wavelength of the line, and a wavelength range is defined based on the input guess for the line FWHM. A set of 50 spectra in this range are generated using a Monte Carlo method and each is fit by a Gaussian. At each step in the Monte Carlo loop, the integrated flux of the line is determined by a weighted average, where the weights follow a Gaussian distribution centered on the observed line centroid and the input line FWHM. With the integrated flux fixed, the velocity of the line centroid is determined. The line fluxes are not corrected for extinction within Pipe3D, so the desired extinction correction can be applied in the analysis. We do not apply an extinction correction, however, because it would have a minimal effect on the line centroid used here. Additional masking was also applied to the CALIFA velocity fields, using an S/N cut based on the integrated flux and error maps. Pixels with S/N <3.5 were blanked.

The linewidths of the V500 data (which covers Hα) are dominated by the instrumental linewidth (6.0 Å ≈ 275 km s^{-1} at $\lambda(H\alpha) = 6562.68$ Å), and hence reliable velocity dispersions are not available for the V500 data. The instrumental linewidth can be removed from the V1200 data (2.3 Å ≈160 km s^{-1} at $\lambda(H\gamma) = 4340.47$ Å). To determine the Hγ linewidth, we start with the continuum-subtracted cube and isolate the Hγ line. We fit the Hγ line at each spaxel using a Gaussian, where the linewidth is given by the width of the Gaussian fit. Pixels with S/N < 3 are blanked. We convert the resulting maps from wavelength to velocity using the relativistic convention, producing maps of the velocity dispersions for each galaxy. Independently, Pipe3D does provide

velocity dispersion maps derived from non-parametric fitting. The values in these maps, however, are frequently lower than the instrumental velocity dispersion over extended regions (a problem we do not find in our Gaussian fitting), and it is known that the pipeline systematically finds dispersions lower than obtained from Gaussian fitting (Section 3.6 of Sánchez et al. 2016c). We compare the velocity dispersions extracted from Pipe3D and our Gaussian fitting to non-parametric fitting done with NEMO (Teuben 1995). In this fitting, we find the linewidth at each spaxel using the ccdmom mom=32 task. This finds the peak, locates the minima on either side of the peak, and takes a second moment over those channels. Velocity dispersions from this method agree much better with the Gaussian fitting results than with the Pipe3D values, hence we adopt the Gaussian fitting results to determine the Hγ velocity dispersion. Before using these velocity dispersion maps in our analysis (Section 5.5.1), we remove the instrumental velocity dispersion, and model and remove the beam smearing effects (the latter is a small effect in the regions where we are interested in measuring the gas velocity dispersion). This procedure is discussed in Appendix B, and further caveats are discussed in Section 5.5.1. We regrid all CALIFA maps to the same grid as the corresponding EDGE map, using the Miriad task regrid (Sault et al. 1995).

CALIFA also derived effective radius (R_e) measurements for all EDGE galaxies as described in Sánchez et al. (2014). These values are listed in Table 4.

When comparing the velocity fields from the EDGE and CALIFA surveys, it is important to note that the velocities are derived using different velocity conventions: EDGE follows the radio convention, and CALIFA follows the optical convention. Because velocities in both surveys are referenced to zero, all velocities are converted to the relativistic velocity convention. In both the optical and radio conventions, the velocity scale is increasingly compressed at larger redshifts; typical systemic velocities in the EDGE-CALIFA sample are ~4500 km s^{-1}. The relativistic convention does not suffer from this compression effect. Differences between these velocity conventions and conversions among them can be found in Appendix A. All velocities presented here are in the relativistic convention, unless otherwise noted.

2.3. Convolving to a Common Spatial Resolution

In order to accurately compare the CO and ionized gas velocity fields, the EDGE and CALIFA data cubes were convolved to the same angular resolution. The convolution was done using the convol task in Miriad (Sault et al. 1995), which uses a Gaussian kernel. The EDGE beam was first circularized by convolving to a value 5% larger than the beam major axis. The CALIFA point spread functions are circular (Sánchez et al. 2016a). The EDGE and CALIFA cubes were convolved to a final 6″ resolution, corresponding to ~2 kpc at the mean distance of the galaxies. Data products were reproduced as outlined in Sections 2.1 and 2.2. The CO and Hα velocity fields for NGC 2347 are shown in Figure 1. The rotation curves were derived as described in Section 3.1. There is excellent agreement between the native and convolved rotation curves for both CO and Hα, suggesting that, while it is best to match physical resolution, the convolution does not affect the results presented here.
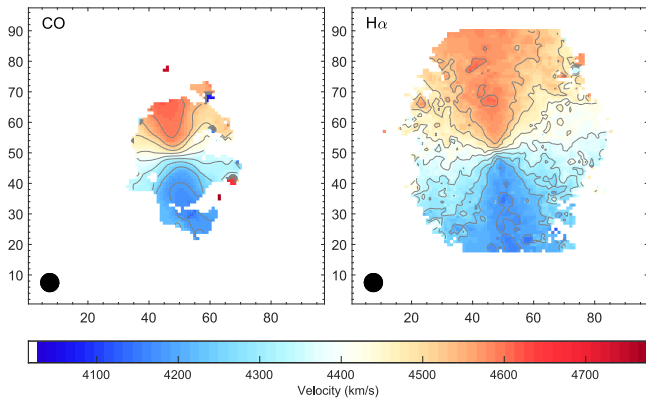
Figure 1. EDGE CO and CALIFA Hα velocity fields convolved to a 6″ beam size for NGC 2347. Isovelocity contours are shown in 50 km s^{-1} increments out to ±250 km s^{-1} from the systemic velocity. The circularized 6″ beams are shown as the black circles.

2.4. GBT H I Data

The EDGE collaboration obtained H I spectra for 112 EDGE galaxies from the Robert C. Byrd Green Bank Telescope (GBT) in the 2015B semester as part of GBT/15B-287 (PI: D. Utomo). We defer detailed discussion of these data to a future paper (T. Wong et al. 2018, in preparation) and here present only a brief overview. Observations were taken using the VEGAS spectrometer with a 100 MHz bandwidth, 3.1 kHz (0.65 km s^{-1}) spectral resolution, and a 3-σ sensitivity of 0.51 mJy. On-source integration time was 15 minutes for each galaxy. The GBT primary beam FWHM was 9′, compared to the average EDGE $D_{25} = 1'.6$, so the galaxies are spatially unresolved. Data were reduced using standard parameters in the observatory-provided GBTIDL package. A first- or second-order baseline was fit to a range of line-free channels spanning 300–500 km s^{-1} on either side of the signal range. The spectra were calibrated to a flux density scale, assuming a gain of 2 K Jy^{-1} and a negligible coupling of the source size to the telescope beam. The widths containing 50% and 90% of the flux (W50 and W90 respectively) were derived from a Hanning smoothed spectrum to use as proxies for the maximum rotation velocity of the neutral atomic gas in these galaxies. These values are listed in Table 1, if available. The H I spectrum for NGC 2347 is shown in Figure 2, with the inclination-corrected W50 and W90 values marked.

If H I data from GBT are not available, only W50 values were taken from Springob et al. (2005). Specifically, we use their W_C values, which are W50 corrected for the instrumental and redshift effects. For this work, these data are used for only three galaxies and come from either the Green Bank 300 ft telescope (NGC 5480 and NGC 5633) or Arecibo (line feed system, UGC 9067). These values are also listed in Table 1.

In this work, we use the H I rotation velocities as point of comparison to the CO and Hα rotation velocities. We convert the W50 and W90 values to rotation velocities where V_{rot}=W /(2 sin i), where i is the galaxy's inclination as listed in Table 3.

3. Data Analysis

3.1. Fitting CO Rotation Curves

Rotation curves were determined for each galaxy using a tilted ring method (Rogstad et al. 1974; Begeman 1989), which has previously been applied to H I data (e.g Begeman 1989; Schoenmakers 1999; Fraternali et al. 2002; de Blok et al. 2008;
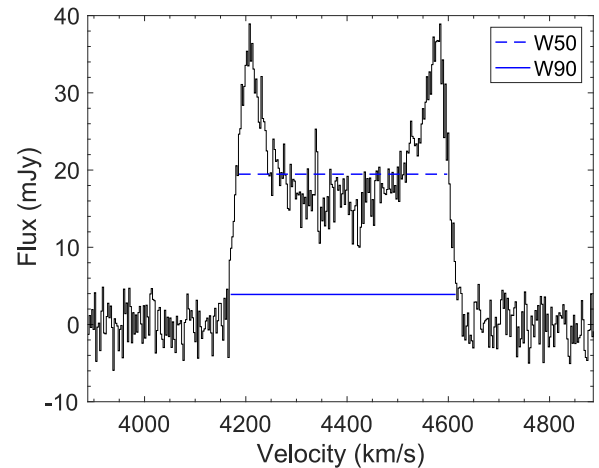

Figure 2. The H I spectrum from the GBT is shown for NGC 2347. The spectrum has been clipped to ±500 km s^{-1} from the CO systemic velocity. The velocities here have been converted to the relativistic convention. Inclination-corrected W50 and W90 values are indicated by the dashed and solid blue lines. For this work, the H I data are used as a comparison to the molecular and ionized gas rotation velocities.

Iorio et al. 2017), ionized gas data (e.g van de Ven & Fathi 2010; Di Teodoro et al. 2016), CO data (e.g Wong et al. 2004; Frank et al. 2016), and recently to [C II]158 μm data in high-redshift galaxies (Jones et al. 2017). Galaxies were deprojected (position angles (PAs) and inclinations are listed in Table 3) and divided into circular annuli. The radius of each annulus was determined such that the width was at least half a beam. The center position, inclination (i), and PA are assumed to be the same for all annuli. The PA takes values between 0° and 360° and increases counterclockwise, where PA = 0 indicates that the approaching side is oriented due north. The rotation (V_{rot}), radial (V_{rad}), and systemic (V_{sys}) velocity components were determined in each ring through a first-order harmonic decomposition of the form

$$V(r) = V_{rot}(r)\cos\psi \sin i + V_{rad}(r)\sin\psi \sin i + \Delta V_{sys}(r),$$
(1)

where r is the galactocentric radius and ψ is the azimuthal angle in the plane of the disk (Begeman 1989; Schoenmakers 1999). Before fitting, the central systemic velocity (V_{sys}^{cen}) was subtracted from the entire map, such that the fitted systemic component is $\Delta V_{sys}(r) = V_{sys}(r) - V_{sys}^{cen}$.

The initial values for the PAs and inclinations were chosen from photometric fits to outer optical isophotes (Falcón-Barroso et al. 2017). If values were not available from this method, they were taken from the HyperLeda database (Makarov et al. 2014). Initial central systemic velocity values (V_{sys}^{cen}) and center coordinates (R.A. and decl.) were taken from HyperLeda. The kinematic PAs were determined from the results of the ring fitting by minimizing V_{rad} at radii larger than twice the CO beam; an incorrect PA will produce a non-zero radial component. The V_{sys}^{cen} values were refined by minimizing ΔV_{sys} at radii larger than twice the CO beam. The inclination is not as easily determined from kinematics; however, examining fits to individual annuli (rather than the rotation curve) can indicate whether the inclination is incorrect. Center offsets in R.A. and decl. (X_{off}, Y_{off}) were determined using a grid search method. At each point in the grid of X_{off} and Y_{off} values, a rotation curve was fit using that center. A constant was fit to the
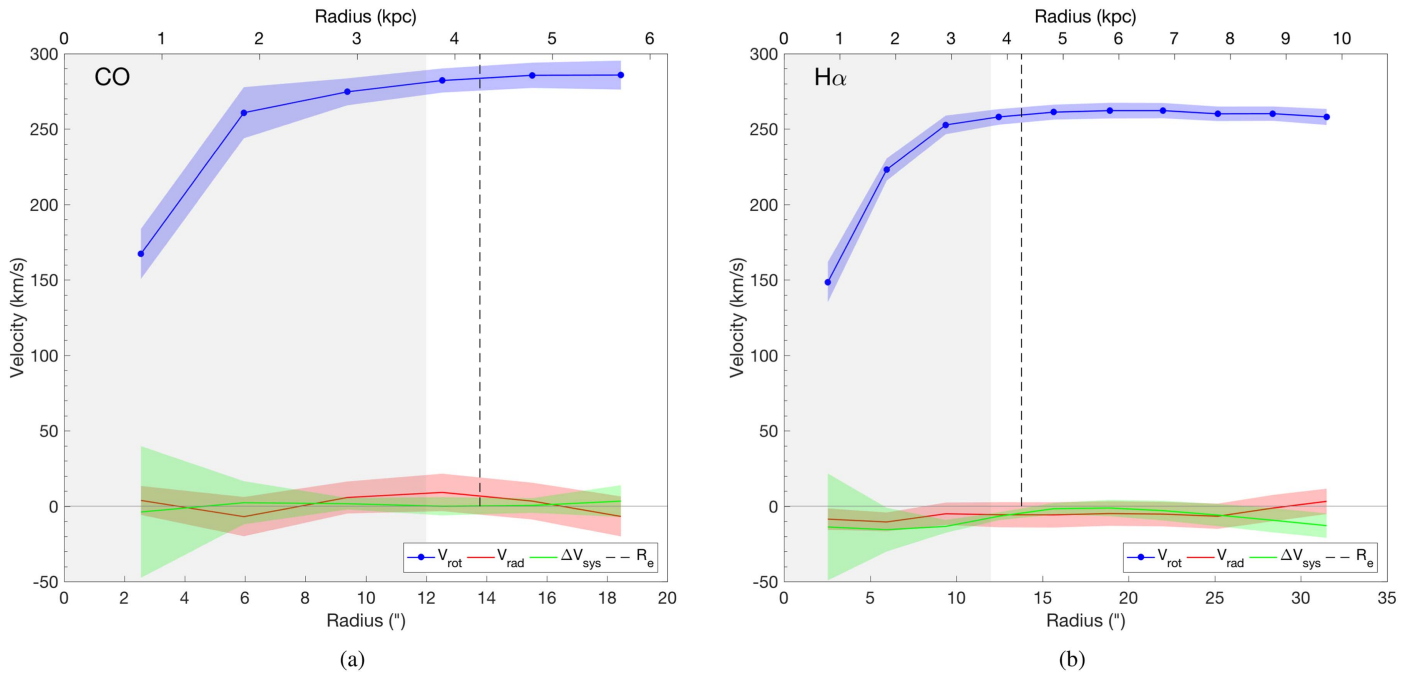
Figure 3. (a) The CO rotation curve for NGC 2347, where V_{rot} is shown in blue, V_{rad} in red, and ΔV_{sys} in green. The colored, shaded regions are the errors on the rotation curve from the Monte Carlo method. The gray-shaded region shows the inner two beams where beam smearing can affect the rotation curve substantially. The black dashed line shows R_e (Table 4). (b) The Hα rotation curve for NGC 2347, where the colors of the curves are the same as (a). In both cases, the V_{rad} and ΔV_{sys} components are small and consistent with zero within the error ranges. The V_{rot} components flatten at larger radii. Interestingly, $V_{rot}(H\alpha)$ is noticeably smaller than $V_{rot}(CO)$.

ΔV_{sys} component, and the combination of X_{off} and Y_{off} resulting in the best fit was selected as the center. The value of V_{sys}^{cen} was then adjusted as necessary to again minimize ΔV_{sys}. The sign of the offset is such that the correct center is $(x_{cen}, y_{cen}) = (\text{R.A.}-X_{off}, \text{decl.}-Y_{off})$. If a rotation curve could not be fit, either because there is little or no detected CO, or because the velocity field is very disturbed, the parameter values were unchanged from the initial values. The final values of the geometric parameters can be found in Table 3, including whether the PA, inclination, and V_{sys}^{cen} values are derived from kinematics (this work), photometrically (Falcón-Barroso et al. 2017), or from HyperLeda.

Errors on the rotation curve were determined using a Monte Carlo method in which the geometrical parameters were drawn randomly from a uniform distribution. The center position was allowed to vary by $1''$ in either direction because the average change in the CO (or Hα) center position from the original value is $0''\!\!.7$ over the whole EDGE sample. The inclination is varied by $2°$, which is the average difference between the final and initial inclinations over the whole EDGE sample. The PA was also allowed to vary by $2°$, which is the median difference between the final and initial PAs over the whole EDGE sample. This allows typical uncertainties in the kinematic parameters to be reflected in the rotation curves. The shaded error regions show the standard deviation of 1000 such rotation curves. The CO rotation curve showing V_{rot}, V_{rad}, and ΔV_{sys} for one galaxy is shown in Figure 3(a).

We note that this method to determine errors on the rotation curve differs from methods that use the differences between the approaching and receding sides of the galaxy, assuming that those differences are at the 2-σ level (e.g., Swaters 1999; de Blok et al. 2008). Typical uncertainties on the CO rotation velocity are $\sim$3–10 km s^{-1} (1-σ). For the uncertainties stemming from the difference in rotation velocity between

the approaching and receding sides to exceed the typical 1σ uncertainties in our Monte Carlo method, we find that rotation velocities of the approaching and receding sides would have to differ by 12–40 km s^{-1}. This seems unlikely, especially given that uncertainties on the rotation velocities derived from the differences between the approaching and receding sides presented by de Blok et al. (2008) are generally $\sim$10 km s^{-1}. Therefore, we conclude that the major sources of uncertainty in deriving our rotation curves are uncertainties in the geometric parameters.

Due to the beam size of the EDGE data, the observed velocities are affected by beam smearing, especially in the centers of the galaxies (Bosma 1978; Begeman 1987). Leung et al. (2018) analyzed the effect of beam smearing in the EDGE sample and found that it is only significant in the inner portions of the galaxy ($\lesssim 0.5\,R_e$) where the velocity gradient is steep. For this study, we do not correct for beam smearing; instead, our analysis excludes points in the rotation curve within two beams from the center. The radius corresponding to twice the CO beam is referred to as R_{2beam} throughout. The excluded central region is shown in gray in Figure 3. Excluding the center of the galaxy also minimizes any effects from a bulge or an active galactic nucleus (AGN).

3.2. Fitting Ionized Gas Rotation Curves

The CALIFA data were fit using the methods described in previous section, as well as the same PA and inclination as the CO listed in Table 3. In some cases, the Hα velocity contours are noticeably offset from the CO contours. CALIFA provides refinements to their astrometry in the headers of the data; however, these refinements are not large enough to account for some observed offsets. The CALIFA pipeline registers the R.A. and decl. for the center of the PPAK IFU to the corresponding
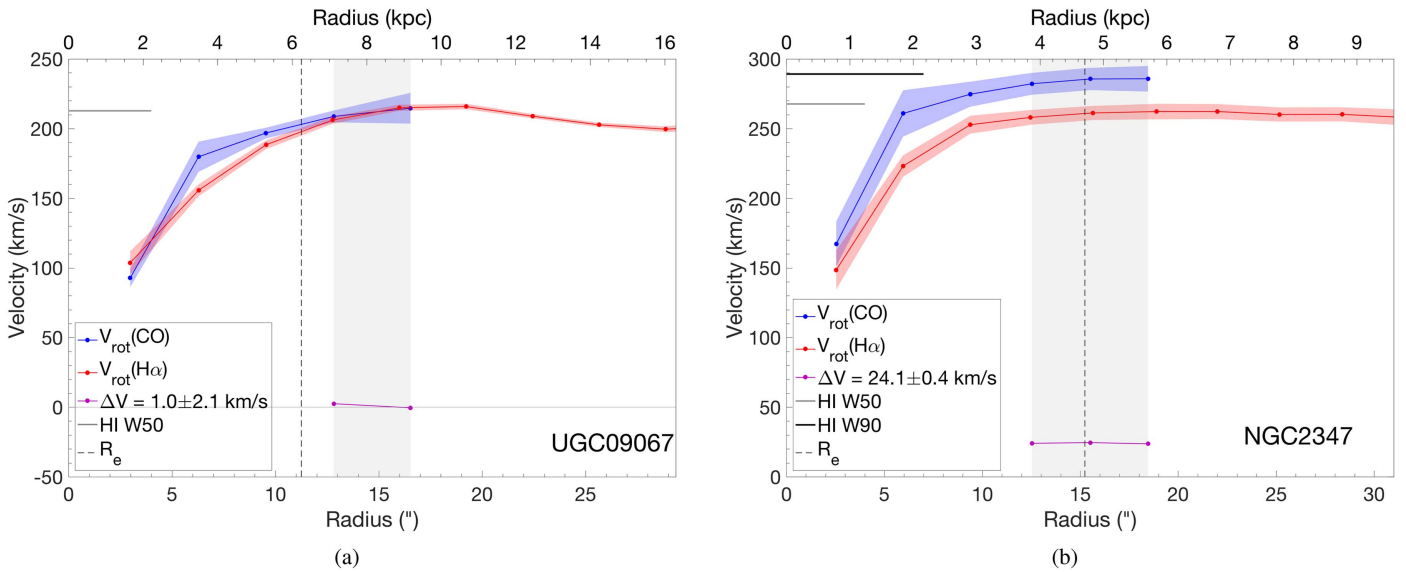
Figure 4. CO and Hα rotation curve comparisons for two galaxies. In both plots, V_{rot}(CO) is in blue and V_{rot}(Hα) is in red. The purple curves show the difference between the rotation curves at radii greater than R_{2beam} to the furthest CO extent. The median difference between V_{rot}(CO) and V_{rot}(Hα) (ΔV) is quoted and the error is the standard deviation. The solid gray and black lines show the inclination-corrected V_{rot}(H I) values from W50 and W90 for comparison. The black dashed lines show R_e (Table 4). (a) UGC 9067 has CO and Hα rotation curves that are consistent within the error bars. (b) NGC 2347 shows a difference of 24 km s^{-1} between the CO and Hα rotation curves. The H I rotation velocities tend to agree better with the CO rotation curve. Many galaxies in the KSS show ΔV larger than the errors on the rotation curves.

center of the SDSS DR7 image (García-Benito et al. 2015). In DR2, 7% of the galaxies have registration offsets from SDSS >3″ (García-Benito et al. 2015). However, this registration process is known to fail in some cases. Indeed, in many of the galaxies for which we find offsets, this registration process has failed. Therefore, CALIFA centers were refit in the same way as the EDGE data, as described in Section 3.1. Because the V500 and V1200 data were taken on different days, the centers of the V500 and V1200 data were refit independently. For both the V500 and V1200 data, the average magnitude of the center offset is 0″.9. The center offsets and V_{sys}^{cen} values for the CALIFA data are presented in Table 4. The Hα rotation curve for NGC 2347 is shown in Figure 3(b).

3.3. The Kinematic Sub-Sample

Of the 126 EDGE galaxies, ≈100 have peak brightness temperatures ⩾5σ (Bolatto et al. 2017). Reliable CO and Hα rotation curves could not, however, be derived for every detected EDGE galaxy. To best compare the CO and Hα rotation curves, a sub-sample of galaxies for which reliable CO and Hα rotation curves could be derived is used for the remainder of the analysis (the Kinematic Sub-Sample or KSS). A reliable rotation curve has small V_{rad} and ΔV_{sys} components at radii larger than R_{2beam} (as in Figure 3). In the centers of galaxies, there may be radial motions due to bars and other effects, but these should not affect the larger radii we consider here. Ensuring that both the CO and Hα have small V_{rad} components validates our assumptions that the CO and Hα have the same PA and inclination and that the PA and inclination do not change much over the disk (i.e., there are no twists or warps). In addition to the criteria on the rotation curves, there are four galaxies (NGC 4676A, NGC 6314, UGC 3973, and UGC 10205) for which the observed CO velocity width may not be fully contained in the band (Bolatto et al. 2017). One galaxy (UGC 10043) has a known Hα outflow (López-Cobá et al. 2017). These galaxies are also excluded from the subsample. Finally, we exclude galaxies with inclinations

larger than 75°. At large inclinations, the line profiles can become skewed and a Gaussian fit to the line profiles is inappropriate and can lead to systematic biases in the mean velocities. We do, however, plan to analyze the highly inclined galaxies in a forthcoming paper (R. C. Levy et al. 2018, in preparation). Under these criteria, our sample size is reduced to 17 galaxies. Figure 18 shows CO and Hα velocity fields and rotation curves for all galaxies in the KSS. Specific notes on each galaxy in the KSS can be found in Appendix C. Table 1 lists global quantities for the KSS not listed in Table 3 or 4.

4. Results

Previous comparisons of molecular and ionized gas rotation velocities for individual galaxies show variations in agreement (e.g., Wong et al. 2004; Simon et al. 2005; Heald et al. 2006a; de Blok et al. 2016). Davis et al. (2013), for example, found that, for 80% of their sample of 24 gas-rich early-type galaxies (ETGs), the ionized gas rotation velocities were lower than for the molecular gas. For a few of the star-forming disk galaxies in our KSS, the molecular and ionized gas rotation velocities agree within the errors, such as UGC 9067 shown in Figure 4(a). The majority of our galaxies, however, have CO rotation velocities measurably higher than the Hα rotation velocities (such as for NGC 2347, shown in Figure 4(b)). In no case is the Hα rotation velocity measurably higher than the CO. To quantify the differences between the CO and Hα rotation curves, the rotational component of the Hα rotation curve was linearly interpolated and resampled at the same radii as the CO rotation curve. We compare V_{rot}(CO) and V_{rot}(Hα) at radii larger than twice the convolved beam (R_{2beam}), to ensure that beam smearing is not affecting the results; the gray-shaded regions in Figure 4 show the radii over which the rotation curves are compared. The differences between V_{rot}(CO) and V_{rot}(Hα) are shown in Figure 4 (purple points). The median of these differences (ΔV) was taken to determine an average velocity difference between the CO and Hα rotational velocities. The
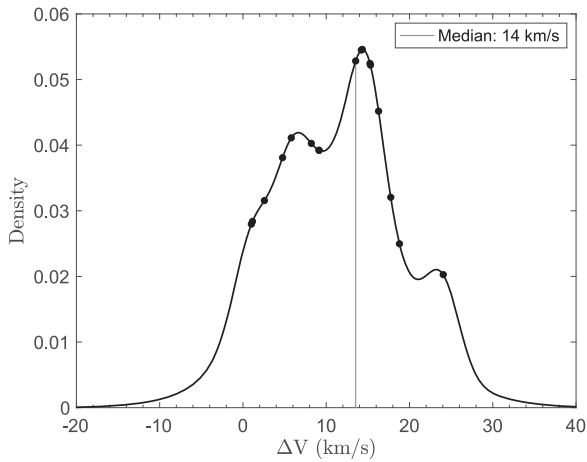
Figure 5. Kernel density estimator showing the distribution of ΔV (the median V_{rot}(CO)–V_{rot}(Hα)) in the KSS. Each galaxy is represented as a Gaussian with centroid $\mu = \Delta V$, $\sigma = \sigma_{\Delta V}$, and unit area. A minimum $\sigma_{\Delta V}$ of 2 km s^{-1} is imposed. The Gaussians are summed to produce a histogram and normalized to unit area. The circles indicate the peak of the Gaussian for each galaxy. All galaxies in the KSS have $\Delta V > 0$. The median ΔV is 14 km s^{-1}.
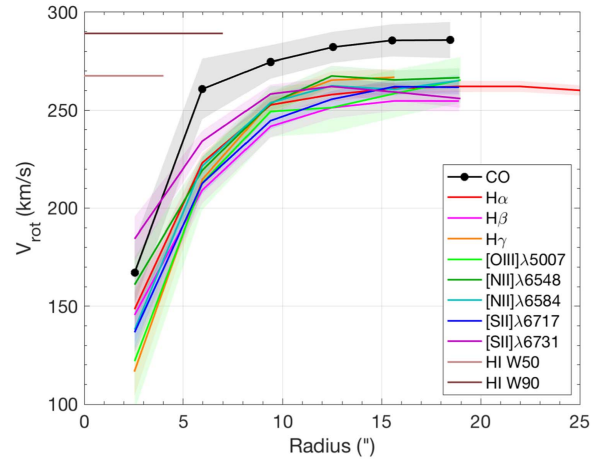

Figure 6. Rotation curves in several ionized gas lines are consistent with each other (using fixed geometric parameters listed in Table 4). The figure shows an example for NGC 2347. For CO, the shaded region shows the error on the rotation curves from variations in the kinematic parameters, using the Monte Carlo method described in Section 3.1. For all other curves, the shaded regions indicate the formal errors from the rotation curve fitting. The rotation curves from the ionized gas are consistent with one another, and all are below the CO rotation curve. Ionized rotation curves other than Hα are truncated at the same radius as CO. The tan and brown horizontal lines show V_{rot}(H I) from W50 and W90 measurements, which tend to agree with the CO rotation velocity. Note that variations among the rotation curves are enhanced because the y-axis does not extend down to zero.

standard deviation of the difference at each radius ($\sigma_{\Delta V}$) is quoted as an error on ΔV. Galaxies have measurably different CO and Hα rotation velocities if $|\Delta V| > \sigma_{\Delta V}$ and are consistent if $|\Delta V| \leqslant \sigma_{\Delta V}$. Of the 17 galaxies in the KSS, $77\%^{+23\%}_{-0\%}$ (13^{+4}_{-0}) show measurably higher CO rotation velocities than Hα, and the other $23\%^{+0\%}_{-23\%}$ (4^{+0}_{-4}) show consistent CO and Hα rotation velocities. This is remarkably similar to the ETG results of Davis et al. (2013).

To better understand the distribution of ΔV in the KSS, a kernel density estimator (KDE) was formed, where each galaxy is represented as a Gaussian with centroid $\mu = \Delta V$, $\sigma = \sigma_{\Delta V}$, and unit area. These Gaussians were summed and re-normalized to unit area. The resulting distribution is illustrated in Figure 5, showing that all galaxies in the KSS have $\Delta V > 0$. The median ΔV of the sample is 14 km s^{-1}.

We find no strong radial trends in ΔV, likely because the range of radii probed is relatively small. Over the 17 KSS galaxies, the median gradient in ΔV with radius is -0.2 ± 6.4 km s^{-1} kpc^{-1}.

In addition to Hα, rotation curves were derived for other ionized lines available from CALIFA using the same method and parameters described in Section 3.2. These lines include Hβ, [O III]λ5007, [N II]λ6548, [N II]λ6583, [S II]λ6717, and [S II]λ6731 from the V500 grating and Hγ from the V1200 grating. Rotation curves from these lines (as well as CO and Hα) are shown for NGC 2347 in Figure 6. All ionized gas rotation curves are below that of CO. The colored shading indicates the errors on the rotation curves; within these errors, the ionized gas rotation curves are consistent with one another. Also shown are the W50 and W90 measurements from the H I data. These values straddle the CO rotation curve, and both are larger than the ionized gas rotation velocities.

The low end of the ΔV values measured by Davis et al. (2013) are comparable to those we measure (Figure 7). Davis et al. (2013) also measure the luminosity-weighted mean EW of Hβ (a measure of the dominance of star formation). CALIFA provides maps of the EW(Hα), and we find the median EW(Hα) in the same region as that where ΔV is calculated (excluding the inner 12″, out to the furthest CO extent). The error is the standard deviation of EWs divided by the square root of the number of beams over the region.

As shown in Figure 8, there is a trend between the EW and ΔV. The EW(Hα) values we measure are larger than those measured by Davis et al. (2013). EWs > 14 Å trace star-forming complexes, and galaxies where the ionization is dominated by H II regions in the midplane tend to have larger EWs (Lacerda et al. 2018). This implies that the bulk of the ionized gas emission in our objects comes from the H II regions in midplane, which naturally rotate at the same velocity as the molecular gas (because they represent recent episodes of star formation). Lacerda et al. (2018) also find that EWs < 3 Å trace regions of diffuse gas ionized by low-mass, evolved stars. These are prevalent in elliptical galaxies and bulges and can also be present above or below the midplane in spirals. EWs between these values are likely produced by a mixture of ionization processes.

This suggests a scenario where ionized gas caused by recent star formation (such as gas associated with H II regions), which is close to the galaxy midplane and has a small scale height, shares the rotation of the molecular gas from which the star formation arose. Ionized gas associated with older stellar populations or produced by cosmic rays (which typically have much larger scale heights), or possibly gas that has been shock-ionized (experiencing an injection of momentum that may drive it to large scale heights) or otherwise vertically transported may rotate at lower speeds.

This scenario is in agreement with the trend seen in Figure 8, in which the ETGs have lower EW(Hβ) and higher ΔV than the star-forming spirals studied here. It also agrees with studies that find vertical gradients in the rotation velocity of the ionized gas in some galaxies (e.g., Rand 1997, 2000). As pointed out by a number of authors, however, the steady-state solution for a homogeneous barotropic fluid immersed in an axisymmetric potential does not allow for such vertical rotation velocity gradients (e.g., Barnabè et al. 2006; Marinacci et al. 2010). Having the ionized disks in equilibrium while maintaining such gradients may require an anisotropic velocity dispersion, similar to what may be expected for a galactic fountain (Marinacci et al. 2010).
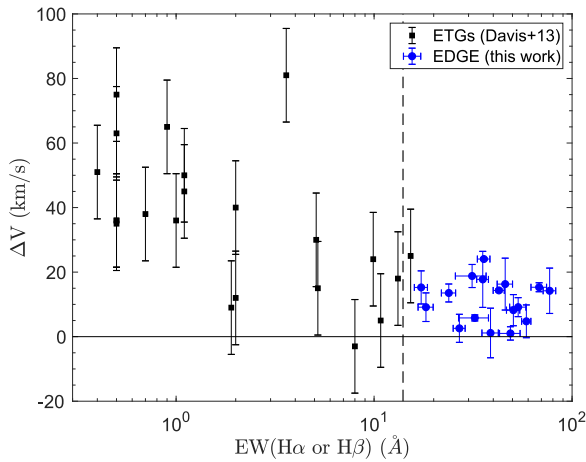
Figure 7. Equivalent width of the Hα or Hβ emission vs. rotation velocity difference between the molecular and ionized gas, ΔV. The blue points are the KSS galaxies, which use EW(Hα). The black points are ETGs from Davis et al. (2013), who use the luminosity-weighted mean EW(Hβ), excluding those that are counter-rotating. Error bars are not provided for the EW(Hβ) data. Our points are consistent with the low ΔV end of the ETGs. EWs >14 Å (vertical dashed line) trace star formation (Lacerda et al. 2018), so it is not surprising that the star-forming disk galaxies used in this study have larger EWs than the ETGs use by Davis et al. (2013).
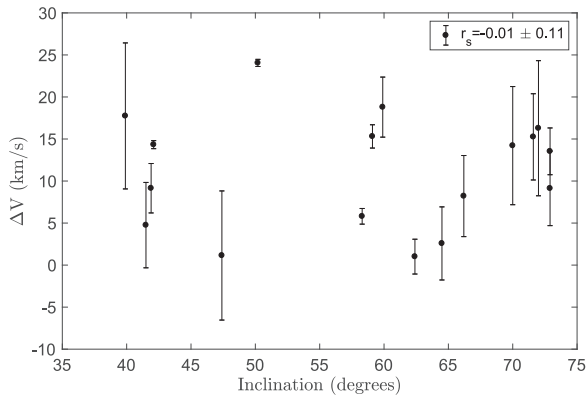

Figure 8. Lack of a trend between galaxy inclination and ΔV. The cause of the observed rotation velocity difference ΔV cannot be purely an inclination effect. The Spearman rank correlation coefficient (r_s) is consistent with 0.

5. Discussion

The ubiquity and magnitude of the differences between the CO and Hα rotation velocities are striking. We propose that these differences could be due to the presence of significant extraplanar diffuse ionized gas (eDIG) in our KSS galaxies. In the following subsections, we give some background on previous eDIG detections, rule out scenarios other than eDIG that could produce this effect, and give support for eDIG in these systems from velocity dispersions and ionized gas line ratios. We also suggest that this thick, pressure-supported disk would have a vertical gradient in the rotation velocity, with gas at higher latitudes rotating more slowly than gas in the midplane.

5.1. Previous Detections of eDIG

eDIG has been observed and discussed in the literature, so we highlight some results here for context. The importance of the warm ionized medium (WIM) as a significant fraction of the ISM in the Milky Way (MW) has been known for over four decades (e.g., Reynolds 1971; Reynolds et al. 1973; Kulkarni

& Heiles 1987; Cox 1989; McKee 1990) and for over two decades in other galaxies (e.g., Dettmar 1990; Rand et al. 1990; Rand 1996; Hoopes et al. 1999; Rossa & Dettmar 2003a, 2003b). In particular, diffuse Hα can contribute >50% of the total Hα luminosity, with large variations (Haffner et al. 2009, and references therein). In the MW, half of the H II is found more than 600 pc from the midplane (Reynolds 1993). How such a large fraction of diffuse gas can be ionized at these large scale heights is debated, but it is widely believed that leaky H II regions containing O-star clusters can produce WIM-like conditions out to large distances from the cluster and the midplane (by taking advantage of chimneys and lines-of-sight with little neutral gas created by past feedback; see Reynolds et al. (2001) and Madsen et al. (2006)), although ionization sources with large penetration depths (such as cosmic rays) or re-accretion from the halo may also play a role.

Extraplanar H I exhibiting differential rotation has been detected in the MW (e.g., Levine et al. 2008) and in studies of individual galaxies (e.g., Swaters et al. 1997; Schaap et al. 2000; Chaves & Irwin 2001; Fraternali et al. 2002, 2005; Zschaechner et al. 2015; Zschaechner & Rand 2015; Vargas et al. 2017). Velocity gradients between the high-latitude gas and the dynamically cold midplane are generally -10–-30 km s^{-1} kpc^{-1}, extending out to a few kpc, but there are large variations among and within individual galaxies.

Extraplanar Hα (i.e., eDIG) has also been found and studied in galaxies, primarily from photometry. In a recent study tracing the WIM in the spiral arms of the MW, Krishnarao et al. (2017) find an offset between the CO and Hα velocity centroids, although they do not interpret this offset as eDIG. Outside the MW, NGC 891 is the prototypical galaxy with bright eDIG extending up to 5.5 kpc from the midplane (Rand et al. 1990; Rand 1997) and a vertical velocity gradient of -15 km s^{-1} kpc^{-1} (Heald et al. 2006a), in agreement with measurements of its extraplanar H I (Swaters et al. 1997; Fraternali et al. 2005). Boettcher et al. (2016) find that the thermal and turbulent velocity dispersions (11 km s^{-1} and 25 km s^{-1}, respectively) are insufficient to support eDIG in hydrostatic equilibrium with a 1 kpc scale height. NGC 5775 has observed H I loops and filaments with their rotation lagging the midplane (Lee et al. 2001), as well as Hα lags of -8 km s^{-1} kpc^{-1} detected up to 6–9 kpc from the midplane (Rand 2000; Heald et al. 2006a). NGC 2403 has eDIG that lags the midplane by 80 km s^{-1}, extending a few kpc above the midplane (Fraternali et al. 2004), in rough agreement with the lags observed in H I, which extend 1–3 kpc from the midplane (Fraternali et al. 2002). Finally, eDIG has been observed in the face-on galaxy M 83 with a lag relative to the midplane of 70 km s^{-1} and a vertical scale height of 1 kpc (Boettcher et al. 2017). There is a range of eDIG velocity gradients and scale heights; moreover, H I and Hα vertical velocity gradients are not always similar or present (e.g., Zschaechner et al. 2015).

Apart from these case studies, there are several large photometric studies of eDIG independent of H I. Following the work of Rand (1996), Miller & Veilleux (2003a) and Rossa & Dettmar (2003a, 2003b) performed larger photometric surveys of nearby edge-on spiral galaxies. Rossa & Dettmar (2003a, 2003b) had a sample of 74 edge-on disks and found that 40.5% of the sample had eDIG extending 1–2 kpc from the midplane. In their sample of 17 galaxies, Miller & Veilleux (2003a) observe eDIG in all but one galaxy. Miller & Veilleux (2003b) did a spectroscopic follow-up study of nine edge-on galaxies with observed eDIG and found vertical velocity gradients ranging from -30 to -70 km s^{-1} kpc^{-1}.

5.2. Comparison with Stellar Dynamical Modeling

The stellar circular velocity curve, which accounts for stellar velocity dispersion, should agree with the CO rotation curve if CO is a dynamically cold tracer. Leung et al. (2018) test three different dynamical models of the galaxy's potential to determine stellar circular velocity curves and compare these to CO rotation curves of 54 EDGE galaxies. Overall, they find agreement between the CO rotation curves and the three models to within 10% at 1 R_e. We defer to Leung et al. (2018) for a complete discussion of the details of the stellar modeling. The agreement between the stellar dynamical modeling and the CO rotation curves verifies that CO is indeed a dynamically cold tracer, indicating that the Hα is exhibiting anomalous behavior rather than the CO. Moreover, our measured CO velocity dispersions (Table 1) are small ($\sim 10\,\mathrm{km\,s^{-1}}$), further indicating that the CO is dynamically cold.

5.3. An Inclined Disk

It is possible that the observed difference between the CO and ionized gas rotation velocities could be produced by the inclination of the disk; however, we find no correlation between ΔV and inclination, as shown in Figure 8. To determine a correlation, we calculate the Spearman rank correlation coefficient (r_s), which quantifies how well the relationship between the variables can be described by any monotonic function. Variables that are perfectly monotonically correlated will have $r_s = \pm 1$, assuming that there are no repeated values of either variable. The Spearman rank correlation coefficient does not, however, take the errors on the data into consideration. The errors on ΔV are especially important here. Therefore, we use a Monte Carlo method to determine the correlation coefficient over 1000 samples drawn from a uniform random distribution within the error ranges on each point. The error reported on r_s is the standard deviation of all 1000 r_s values. As shown in Figure 8, the difference between the CO and Hα rotation velocities is not a result of the inclination of the galaxy ($r_s = -0.01 \pm 0.11$).

We note that, if the molecular and ionized gas disks had different inclinations, our assumption that they are the same could produce a ΔV. However, to produce only $\Delta V > 0$ would require that all ionized gas disks are less highly inclined (with respect to us) than the molecular gas disks, which is extremely unlikely for a sample of 17 galaxies. We can, therefore, rule out that the inclination affects the results in this way.

We also plotted ΔV against other global parameters of the galaxies, such as stellar mass (M_*), SFR, specific SFR (sSFR $\equiv$ SFR/M_*), morphology, physical resolution, and CO V_{max}. There are no trends with any of these global parameters, but they are shown for completeness in Figure 17 of Appendix C. As mentioned in Section 2.3, the lack of trend with physical resolution (Figure 17(e)) justifies our choice to convolve to a common angular resolution rather than to a common physical resolution. These values and their sources are listed in Table 1. The lack of trends with these parameters agrees with Rossa & Dettmar (2003b), who also found no trends in the presence of eDIG with such global parameters.

5.4. SFR Surface Density Threshold

In previous studies of eDIG, Rand (1996) and (Rossa & Dettmar 2003a) found a possible trend in the amount of eDIG with the SFR per unit area (Σ_{SFR}) as traced by the far-infrared (FIR) luminosity (L_{FIR}). The physical picture is that a minimum
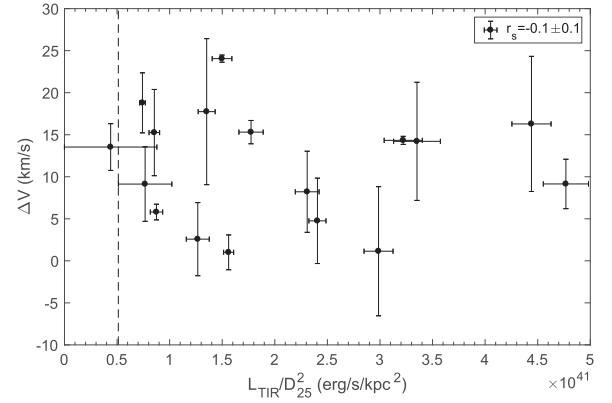

Figure 9. L_{TIR}/D_{25}^2 vs. ΔV for the KSS. The vertical dashed line shows the eDIG threshold from Rossa & Dettmar (2003a) of $L_{TIR}/D_{25}^2 = 5.1 \times 10^{40}\,\mathrm{erg\,s^{-1}}$ (Equation (3)). We find that >90% of our sample exceed this threshold, indicating the likely presence of eDIG in these systems. There is not, however, a trend between L_{TIR}/D_{25}^2 and ΔV.

level of widespread star formation is needed to sustain a thick disk that covers the entire plane of the galaxy. Rossa & Dettmar (2003a) determine a threshold Σ_{SFR} above which they claim that an eDIG will be ubiquitous. This does not guarantee, however, that galaxies above this threshold will always have an eDIG or that galaxies below it cannot have eDIG. Rossa & Dettmar (2003a) define this threshold Σ_{SFR} as

$$\frac{L_{FIR}}{D_{25}^2} = (3.2 \pm 0.5) \times 10^{40}\mathrm{erg\,s^{-1}\,kpc^{-2}}, \qquad (2)$$

where D_{25} is diameter of the 25th magnitude isophote. Catalán-Torrecilla et al. (2015) measure total IR (TIR, 8–1000 μm) luminosities (L_{TIR}) for 272 CALIFA galaxies, and L_{TIR} measurements are available for 15/17 KSS galaxies. The threshold defined by Rossa & Dettmar (2003a) can be converted to TIR by multiplying by 1.6 (Sanders & Mirabel 1996), such that

$$\frac{L_{TIR}}{D_{25}^2} = (5.1 \pm 0.8) \times 10^{40}\mathrm{erg\,s^{-1}\,kpc^{-2}}. \qquad (3)$$

For the two galaxies without L_{TIR} measurements, we can estimate L_{TIR} from the SFR measured by CALIFA from extinction-corrected Hα, where

$$L_{TIR} = \frac{1.6}{4.5 \times 10^{-44}}\left[\frac{\mathrm{SFR}}{M_\odot\,\mathrm{yr^{-1}}}\right]\mathrm{erg\,s^{-1}} \qquad (4)$$

(Kennicutt 1998) and the factor of 1.6 comes from converting from L_{FIR} to L_{TIR} (Sanders & Mirabel 1996). Using measurements of D_{25} from HyperLeda (values are listed in Table 1), we compare the values of L_{TIR}/D_{25}^2 for all KSS galaxies to the eDIG threshold (Equation (3)) in Figure 9. We find that $94^{+6}_{-0}\%$ of galaxies in the KSS have L_{TIR}/D_{25}^2 greater than this threshold and should have eDIG based on this criterion.

If many galaxies have a thick ionized disk, this could underestimate the dynamical mass of the galaxy derived from the ionized gas rotation velocity. Because we find that the ionized gas rotates more slowly than the molecular gas in galaxies with large Σ_{SFR}, this effect could be significant in local star-forming galaxies, and even more so at higher redshifts where there is more star formation occurring on average.
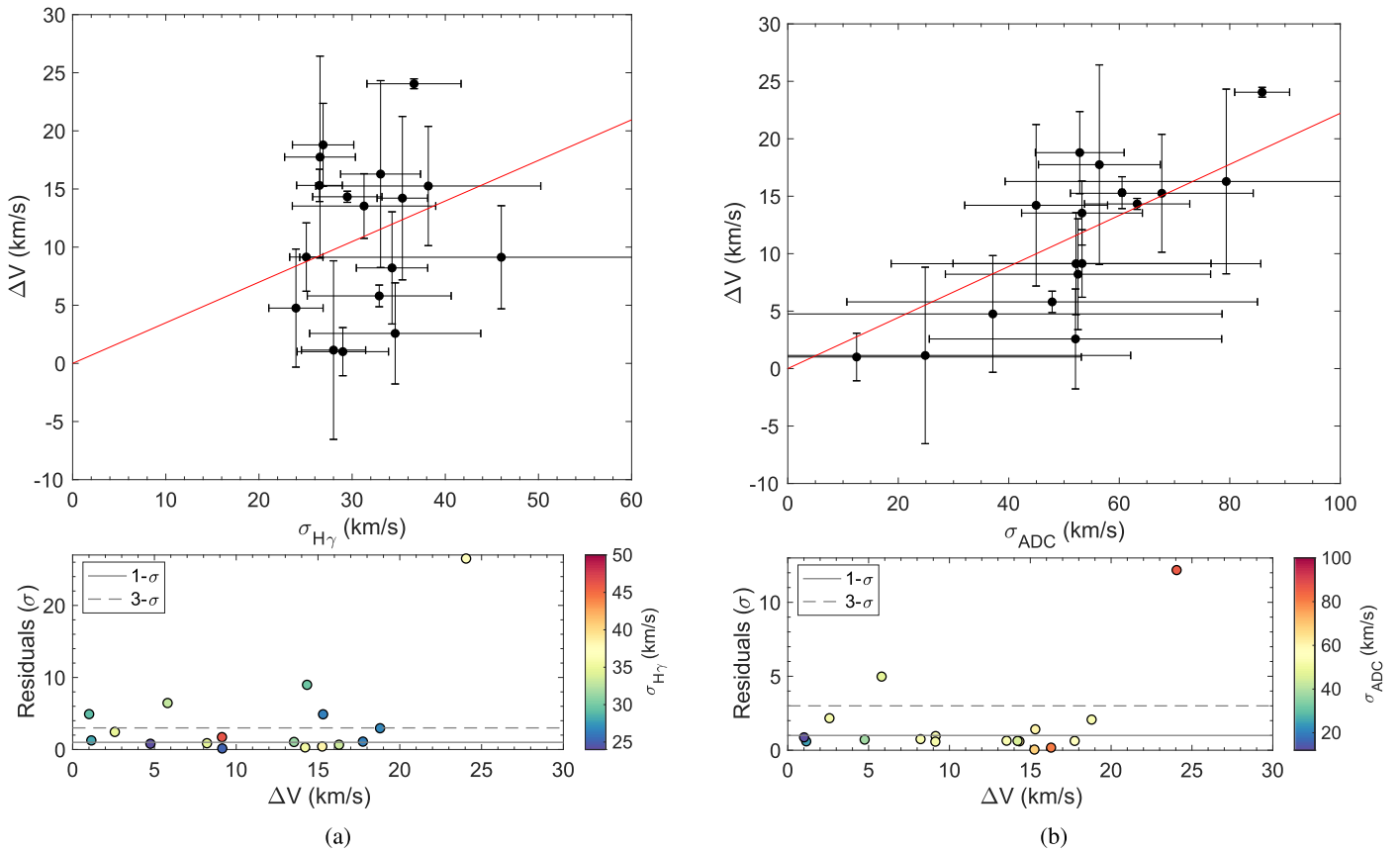
10

Figure 10. (a) The top panel shows the trend between the velocity dispersion measured from the Hγ linewidth ($\sigma_{H\gamma}$) and ΔV. Error bars reflect the propagated error. The red line is a linear fit to the data points. The lower panel shows the perpendicular distance of each point from the line in units of standard deviations plotted against ΔV. Points are color-coded by σ_{ADC}. The solid and dashed gray lines show one- and three-sigma. Thirty-five percent of the galaxies are within 1σ of the best-fit line and 71% are within 3σ. If there is an underlying correlation between $\sigma_{H\gamma}$ and ΔV, it is weak. (b) The same as (a), but using the velocity dispersions inferred from the ADC (σ_{ADC}). The trend results from the form of the ADC used here (Equation (6)). Seventy-one percent of the galaxies are consistent with the best-fit line within 1σ and 88% are consistent within 3σ. In both bottom panels, the galaxy many σ away from the best-fit line is NGC 2347.

5.5. Ionized Gas Velocity Dispersion

The trends between the eDIG and the SFR surface density discussed in Section 5.4 (e.g., Rand 1996; Rossa & Dettmar 2003a) are suggestive of star formation feedback playing an important role in forming the eDIG. In order for ionized gas to remain above or below the disk midplane in a long-lived configuration, it must have sufficient velocity dispersion (or at least a vertical bulk motion). This effectively acts as as an additional pressure term, allowing the gas to remain at larger scale heights. Therefore, we expect that galaxies with larger ionized gas velocity dispersions should have larger eDIG scale heights. Measuring the ionized gas velocity dispersion is, therefore, an important way to test these ideas.

5.5.1. Hγ Velocity Dispersion Measurements

CALIFA data cannot, unfortunately, be used to accurately measure the Hα linewidth due to the low spectral resolution of the V500 grating employed (6.0 Å FWHM ≈ 275 km s^{-1} at Hα). CALIFA observes Hγ with the moderate-resolution V1200 grating (2.3 Å FWHM ≈ 160 km s^{-1} at Hγ), however, and those data can be used, in principle, to establish ionized gas velocity dispersions. Starting with the continuum-subtracted cubes, we fit the Hγ line with a Gaussian at each spaxel where the width of the Gaussian corresponds to the velocity dispersion, as discussed in

Section 2.2. The measured linewidth is the convolution of the instrumental response with the actual gas velocity dispersion; with a small contribution from rotation smearing caused by the finite angular resolution. We apply a beam smearing correction that also accounts for the instrumental velocity dispersion. This method is described in detail in Appendix B. The accuracy of the resulting ionized gas velocity dispersion depends critically on our exact knowledge of the spectral resolution and response of the grating, because the instrumental velocity dispersion ($\sigma_{inst} \approx 68$ km s^{-1}) is of the same order as the observed $\sigma_{H\gamma}$ before removal: in other words, the spectral resolution of the V1200 observation is marginal for the purposes of measuring the velocity dispersion in these galaxies, and our results should be considered tentative. Inspection of the maps suggests that it is likely that the beam smearing corrected $\sigma_{H\gamma}$ values reported here are lower limits to the real ionized gas velocity dispersion, and we caution against over-interpretation of these values. We do not correct our $\sigma_{H\gamma}$ for inclination, and hence assume that the velocity dispersion is isotropic. As discussed in Section 4, anisotropic velocity dispersions may be required to maintain ionized gas disks with vertical gradients in the rotation velocity (Marinacci et al. 2010). With these caveats in mind, we calculate the average beam smearing corrected Hγ velocity dispersion over the same region where ΔV is calculated. Velocity dispersions range from ∼25–45 km s^{-1} (Figure 10(a)). The scale height of the disk (h)

corresponding to a given isotropic velocity dispersion (σ) is

$$h = \frac{\sigma^2}{\pi G \Sigma_*(r)} \quad (5)$$

(van der Kruit 1988; Burkert et al. 2010). We use azimuthally averaged radial profiles of the stellar surface density (Σ_*) from Utomo et al. (2017) to find Σ_* over the same range of radii where ΔV is calculated (listed in Table 1). The scale heights that correspond to the observed $\sigma_{H\gamma}$ are $\sim$0.1–1.3 kpc. Previous measurements of eDIG scale heights range from 1 to 2 kpc (Miller & Veilleux 2003b; Rossa & Dettmar 2003a; Fraternali et al. 2004) up to a few kpc above the disk (Rand 2000, 1997; Miller & Veilleux 2003a). Because our $\sigma_{H\gamma}$ are likely lower limits, the scale heights may indeed be larger than we report here.

5.5.2. Velocity Dispersion Estimates from an Asymmetric Drift Correction (ADC)

It is possible to infer the velocity dispersion needed to produce the observed ΔV using an ADC. Generally, an ADC is used to find V_{circ} given V_{rot}, σ, and $\Sigma_*(r)$; however, because V_{rot}(CO) traces V_{circ} (Section 5.2), we can invert the ADC to find σ instead, with $V_{rot} = V_{rot}(H\alpha)$. If we assume that the velocity dispersion is isotropic ($\sigma_r = \sigma_z = \sigma_\phi$), $\sigma(r) =$ constant, and $\Sigma_*(r) = 2\rho(r, z)h(z)$ (Binney & Tremaine 2008), then

$$\sigma^2 = \frac{V_{circ}^2 - V_{rot}^2}{-d\ln\Sigma_*/d\ln r}. \quad (6)$$

We use azimuthally averaged radial profiles for $\Sigma_*(r)$ from Utomo et al. (2017) to find $d\ln\Sigma_*/d\ln r$. We average V_{circ}, V_{rot}, and $\Sigma_*(r)$ over the same radii as those where ΔV is calculated; this excludes the central two beams ($12'' \sim 4$ kpc) where beam smearing or a bulge can affect the rotation curve. Velocity dispersions from the ADC method (σ_{ADC}, Equation (6)) range from $\sim$15–85 km s^{-1} in the KSS (Figure 10(b)). There is an apparent trend with ΔV resulting from Equation (6). Using Equation (5), we find scale heights ranging from $\sim$0.1 to 2.0 kpc, again in rough agreement with previous measurements. For individual galaxies, the velocity dispersions and scale heights predicted from the ADC tend to be larger than those measured in the Hγ (Figure 11), but given the difficulty in the measurement, the agreement is reasonable.

5.5.3. Trends between ΔV and the Velocity Dispersion

To explain the difference in rotation velocities observed between the molecular and ionized gas as resulting from the presence of eDIG, we would expect that galaxies with a larger ΔV should have larger velocity dispersions as well. There is a trend between ΔV and σ_{ADC} (Figure 10(b)) stemming directly from the form of the ADC used (Equation (6)). There is not, however, an immediately apparent relation between ΔV and $\sigma_{H\gamma}$ (Figure 10(a)). Because the errors on both ΔV and $\sigma_{H\gamma}$ are large, however, there could be an underlying correlation. To assess whether an underlying correlation could exist, we fit a line to the data points (top panels of Figure 10). We then calculate the perpendicular distance of each point from the line, as well as the error on that distance accounting for the error
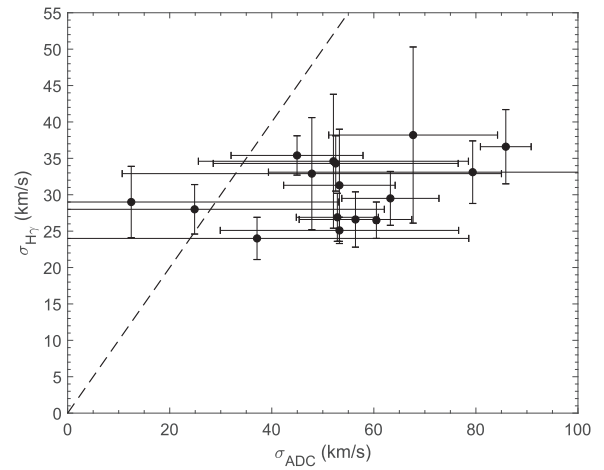

Figure 11. The velocity dispersions inferred from the ADC, compared to those measured for the Hγ emission in each galaxy. The error bars reflect the statistical errors, measured from the standard deviation of the measurements in the annulus. The dashed line is one-to-one. The velocity dispersion $\sigma_{H\gamma}$ is roughly comparable to those inferred from the σ_{ADC}; although $\sigma_{H\gamma}$ tends to be smaller than σ_{ADC}, this should not be over-interpreted, given the difficulty of the measurement discussed in Section 5.5.1.

bars on both quantities. From this, we determine the distance from the best-fit line in standard deviations (bottom panels of Figure 10). For the ADC, 71% of the galaxies are consistent with the best-fit line within 1σ and 88% are consistent within 3σ (Figure 10(a)). This tight correlation again stems from the form of the ADC used, because σ_{ADC} depends explicitly on $\sqrt{V_{rot}(CO)^2 - V_{rot}(H\alpha)^2}$, which is $\sim\sqrt{V_{rot}\Delta V}$ (Equation (6)). For $\sigma_{H\gamma}$, however, only 35% of the galaxies are within 1σ of the best-fit line and 71% are within 3σ (Figure 10(a)), so any underlying correlation between $\sigma_{H\gamma}$ and ΔV is weak. Nonetheless, most of our galaxies have high enough velocity dispersions to support a thick ionized gas disk, and nearly all of our subsample have sufficient Σ_{SFR} (Figure 9).

5.6. [S II]/Hα and [N II]/Hα Ratios

The velocity dispersion is not the only tracer of eDIG. The ratios of [N II]λ6583/Hα ([N II]/Hα) and [S II]λ6717/Hα ([S II]/Hα) increase with distance from the midplane and are used to probe the ionization conditions of the WIM (e.g., Miller & Veilleux 2003a, 2003b; Fraternali et al. 2004; Haffner et al. 2009). Although [S II]/Hα varies only slightly with temperature, [N II]/Hα is used to trace variations in the excitation temperature of the gas (Haffner et al. 2009). From observations of the MW and a few other galaxies, [S II]/Hα = 0.11 $\pm$ 0.03 and [N II]/H$\alpha \sim$ 0.25 in the midplane (Madsen 2004; Madsen et al. 2006), whereas [S II]/Hα = 0.34 $\pm$ 0.13 and [N II]/H$\alpha \gtrsim$ 0.5 in the eDIG (Madsen 2004; Blanc et al. 2009). Observations of these ratios indicate that there must be additional heating sources aside from photoionization from leaky H II regions to produce the WIM (Haffner et al. 2009, and references therein).

CALIFA provides Hα, [S II], and [N II] intensity maps for all galaxies. These were masked to cover the same radii as those where ΔV is calculated. As shown in Figure 12, there are no trends between [S II]/Hα or [N II]/Hα with ΔV ($r_s = 0.03 \pm 0.18$ and $r_s = -0.02 \pm 0.17$, respectively). For both [S II]/Hα
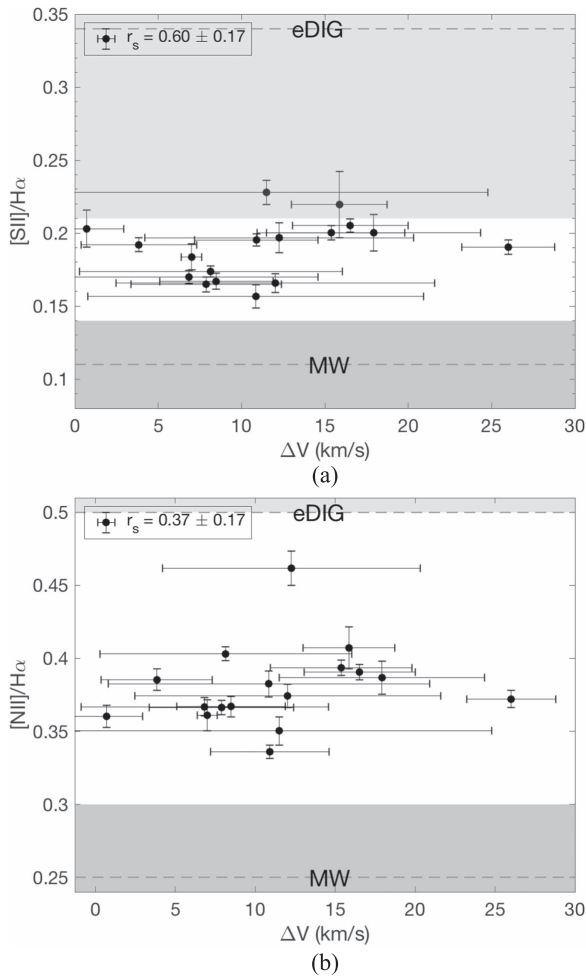
Figure 12. (a) There is no trend between ΔV and [S II]/Hα, although the errors bars are large. All of our [S II]/Hα ratios are larger here than for the MW (dark gray-shaded region, [S II]/H$\alpha = 0.11 \pm 0.03$), but only a few fall within the observed range for the eDIG (light gray-shaded region, [S II]/H$\alpha = 0.34 \pm 0.13$). The dashed gray lines show the median values for the MW and eDIG. (b) There is no trend between [N II]/Hα and ΔV. As with [S II]/Hα, all of our measured ratios exceed those found in the plane of the MW (dark gray-shaded region, [N II]/H$\alpha \sim 0.25$ where we have adopted a 20% error range), but are not as high as is generally observed in the eDIG (light gray-shaded region, [N II]/H$\alpha \gtrsim 0.5$). The dashed gray lines show the median values for the MW and eDIG.

and [N II]/Hα, our ratios are all larger than for the plane of the MW, but only a few fall within the observed range for the eDIG. This is perhaps not unexpected, because emission from the plane is mixed with emission from the eDIG that would systematically lower the observed ratios. This is an encouraging hint that the observed ΔV could be due to eDIG in a thick disk.

5.7. Kinematic Simulations

To further investigate how the disk's geometry affects the observed rotation curve, we perform a suite of kinematic simulations using NEMO. Disks are given different scale heights and vertical rotation velocity distributions, as described in the follow subsections. The particle velocities are given by an input rotation curve that rises linearly from $r = 0$–1 units and is constant at $V_0 = 200$ km s^{-1} from $r = 1$–6 units. The disk is then inclined and "observed" with a one-unit beam. The

velocity is derived by fitting the peak of the line at each point in the simulated data cube. We then average $V_{\rm rot}(r)$ between $r = 1$ and $r = 5$, in order to give $\bar{V}$ in the flat part of the rotation curve. The error on $\bar{V}$ ($\sigma_{\bar{V}}$) is the standard deviation of $V_{\rm rot}(r)$. A simulated ΔV is computed by $V_0 - \bar{V}$, which is analogous to the ΔV defined previously (V_0 corresponds to $V_{\rm rot}({\rm CO})$ and $\bar{V}$ corresponds to the median $V_{\rm rot}({\rm H}\alpha)$ in the outer part of the galaxy). We test four disk configurations, which are described below. To convert the scale heights to physical units (i.e., kpc), we use the turn-over radius (R_0) of the rotation curve (one unit in the simulations) and find the average R_0 of the KSS Hα data. We fit the KSS Hα rotation curves with $V_{\rm model} = V_0(1 - e^{-R/R_0})$ (e.g., Boissier et al. 2003; Leroy et al. 2008) and fix V_0 to the value determined for that galaxy. The average R_0 over the sample is found, and the scaling is one unit = 1.77 ± 0.25 kpc. We note that the assumed beam in the simulations is one unit, which is nearly identical to the beam size of the observations ($6'' = 1.73$ kpc at the average distance of the KSS galaxies).

5.7.1. Thin Disks

First, we create a thin disk of particles with scale height $h = 0$. The simulated ΔV as a function of inclination is shown in Figure 13(a). The resulting ΔV values are all very small and are insufficient to explain the offsets seen in Figure 5. We recover the input rotation curve to within ~ 2 km s^{-1}. This ~ 2 km s^{-1} offset is due to beam smearing. If a smaller beam is used, this offset disappears. Ergo, neither the inclination nor beam smearing of a thin disk can produce the observed ΔV.

5.7.2. Thick Disks

Using the same simulation setup described above, the initial disk can be given a scale height. The same input rotation curve is used at all heights, z, such that $V_{\rm rot}(r, z) = V_{\rm rot}(r, z = 0) = V_0$. Particles are distributed vertically, using a Gaussian distribution where the FWHM is $2\sqrt{2\ln 2}\, h$ (so the scale height above the midplane is h). We then calculate ΔV from these simulations, as described previously. Figure 13(b) shows ΔV as a function of h, color-coded by inclination. There is only a trend for the highest inclinations, and even at these high inclinations, ΔV is not as large as many galaxies in the KSS. Therefore, a thick disk with $V_{\rm rot}(z) = V_0$ cannot cause the observed ΔV, except perhaps for very highly inclined galaxies. For intermediate inclinations, we again recover the input rotation curve to within the ~ 2 km s^{-1} from beam smearing.

5.7.3. Thick Disks with Vertical Rotation Velocity Gradients

We also test a thick disk with a vertical gradient in the rotation velocity. As mentioned in Section 5.1, vertical gradients in the rotation velocity have been observed in the extraplanar H I and eDIG of several galaxies. The physical rationale behind a vertical gradient in the rotation velocity is related to turbulent pressure support. Gas with larger velocity dispersions can be in pressure equilibrium at larger distances from the disk midplane. Material off the plane should have an orbit inclined with respect to the main disk enclosing the galactic center (like the stars); however, pressure support forces the gas to orbit parallel to the main disk. The gas farther off the plane rotates more slowly than gas closer to the plane, creating the vertical gradient in the rotation velocity. First, we impose a linear vertical rotation velocity gradient parameterized by η,
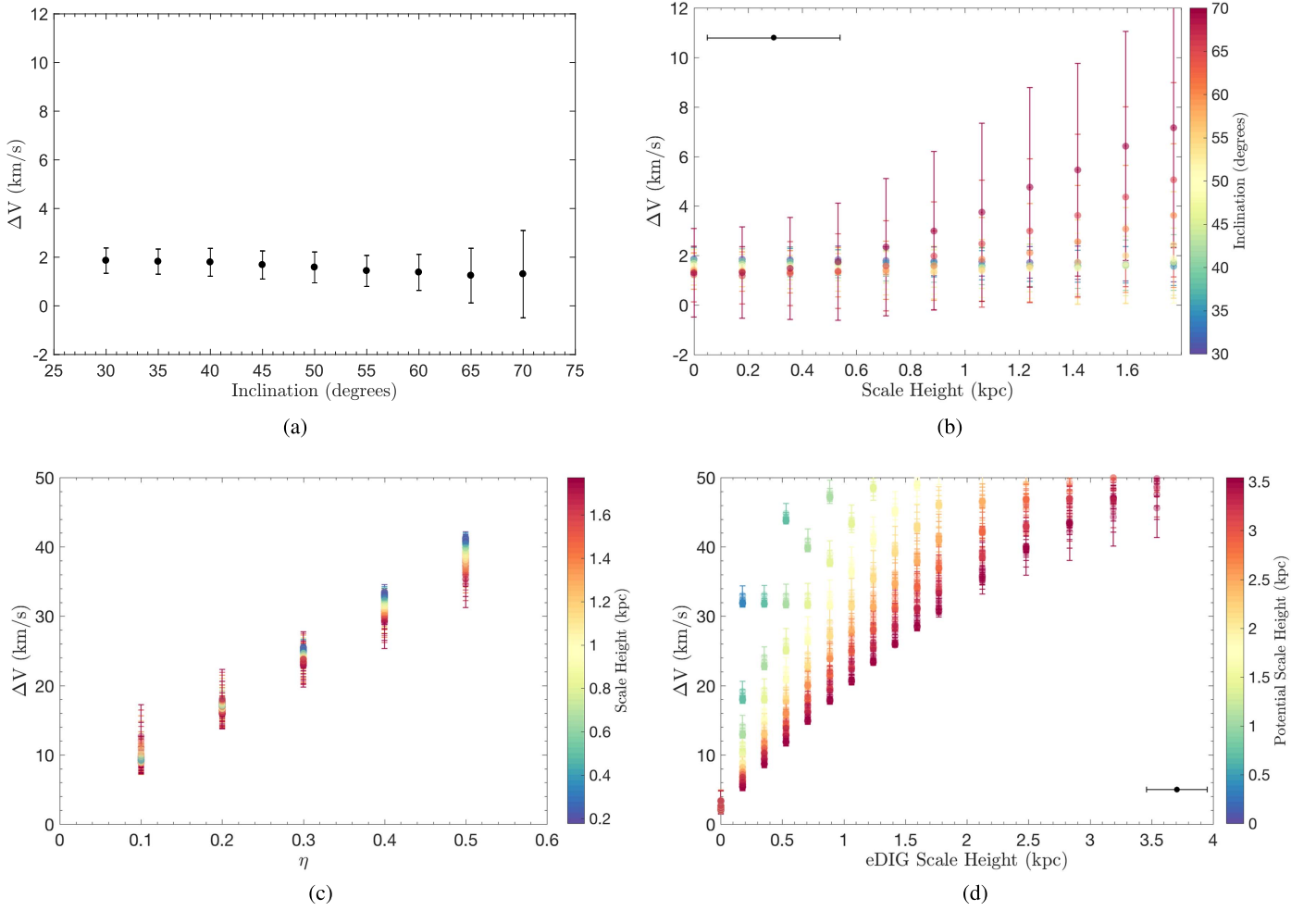
(a)

(b)

(c)

(d)

Figure 13. (a) From the simulations of thin inclined disks, the ΔV values are all very small, so inclination cannot explain the observed ΔV. The $\sim$2 km s^{-1} offset away from $\Delta V = 0$ is due entirely to beam smearing. (b) From the simulations of thick disks with no vertical rotation velocity gradient (i.e., $V_{\rm rot}(z) = V_0$), there is no trend between ΔV and the scale height. There is only a trend for the most highly inclined galaxies (and the errors are large). Ergo, a thick disk without a vertical rotation velocity gradient cannot explain the ΔV measured in all systems. Again, the constant offset away from $\Delta V = 0$ is due entirely to beam smearing. The black point in the upper left corner shows the error on the scale height from the scaling between units in the simulation to kpc. Points are color-coded based on their inclination. (c) For a thick disk with a linear vertical rotation velocity gradient, there is a strong trend between the magnitude of the gradient (parameterized by η, see Equation (7)) and ΔV, producing ΔV values comparable to those observed for $\eta \lesssim 0.3$. Points are color-coded based on the scale height. (d) Using the more realistic model with $V_{\rm rot}(r, z)$ given by Equation (12) and $\rho_{\rm eDIG}(z)$ given by Equation (13), we find that there is a strong trend between the eDIG scale height ($h_{\rm eDIG}$) and ΔV. It is possible to produce ΔV in the range we observe (5–25 km s^{-1}) with $h_{\rm eDIG} \lesssim 1.5$ kpc. There is also a trend with the scale height of the underlying potential (h_p, shown in the color-coding), but this trend is weaker. The black point in the lower right corner shows the error on the scale height from the scaling between units in the simulation to kpc.

where

$$V_{\rm rot}(z) = V_0\left(1 - \eta\frac{z}{h}\right). \qquad (7)$$

As shown in Figure 13(c), there is a strong trend between η and ΔV. A linear vertical gradient in the rotation velocity can produce the observed values of ΔV for $\eta \lesssim 0.3$, meaning that at $z = h$, $V_{\rm rot} \gtrsim 0.7V_0$. For a given value of η, larger scale heights have less of an effect on ΔV, as seen from their shallower slope in Figure 13(c).

Next, we test a more realistic model for $V_{\rm rot}(z)$ than the linear vertical velocity gradient. The rotation velocity of material above the disk is governed by the potential. Here, we assume that the rotation velocity in the disk midplane is constant (V_0),

hence the radial surface density profile, $\Sigma(r)$, is described by a Mestel disk (Mestel 1963; Binney & Tremaine 2008). We also assume that the vertical density distribution is exponential. Therefore, the total density distribution of material that dominates the potential has the form

$$\rho(r, z) = \frac{V_0^2}{2\pi Grh_p}e^{-|z|/h_p}, \qquad (8)$$

where h_p is the vertical scale height of the material that dominates the potential. The potential of a thin Mestel disk is

$$\phi(r) = -V_0^2\ln\left(\frac{r}{r_{\rm max}}\right), \qquad (9)$$

where r_{max} is the maximum extent of the disk (Binney & Tremaine 2008). Therefore, the total potential is

$$\phi(r, z) = \int \phi(r, z - z')\xi(z')dz'$$

$$= -V_0^2 \ln\left(\frac{r}{r_{max}}\right)\frac{1}{h_p} \int e^{-|z'|/h_p}dz'$$

$$= V_0^2 \ln\left(\frac{r}{r_{max}}\right)e^{-|z|/h_p} + c, \qquad (10)$$

where the constant of integration (c) can be found by demanding that $\phi(r, z \to \infty) \to 0$. Therefore,

$$\phi(r, z) = V_0^2 \ln\left(\frac{r}{r_{max}}\right)e^{-|z|/h_p}. \qquad (11)$$

The rotation velocity from a potential is given by $V_{rot}^2 = r\frac{\partial}{\partial r}\phi(r, z)$ (Binney & Tremaine 2008). Thus, from Equation (11),

$$V_{rot}(r, z) = V_0\sqrt{e^{-|z|/h_p}}, \qquad (12)$$

where the absolute value preserves the symmetry above and below the disk. The eDIG has its own density distribution and scale height (h_{eDIG}), which are largely independent of the potential and determined mostly by the star formation activity. Although large ratios of h_{eDIG}/h_p are physically unlikely, here we treat these two scale heights as independent quantities. We can find the eDIG density as a function of z where the vertical density distribution is described by the hydrostatic Spitzer solution (Spitzer 1942; Binney & Tremaine 2008; Burkert et al. 2010):

$$\rho_{eDIG}(r, z) = \rho_0 \operatorname{sech}^2\left(\frac{z}{h_{eDIG}}\right), \qquad (13)$$

where ρ_0 is the density in the midplane. We repeat the NEMO simulations as before, but using $V_{rot}(r, z)$ given by Equation (12) (rather than Equation (7)) and an eDIG density distribution give by Equation (13) (rather than a Gaussian). The results of this more realistic model are shown in Figure 13(d). There is a strong trend between h_{eDIG} and ΔV. There is also a secondary trend between h_p and ΔV. With this model, it is possible to reproduce the observed range of ΔV with $h_{eDIG} \lesssim$ 1.5 kpc. Using Equation (5) and the median Σ_* of the KSS at the radius where the measurements are done (≈ 200 M$_\odot$ pc^{-2}), this implies a velocity dispersion $\lesssim 60$ km s^{-1}, which agrees with the range of velocity dispersions inferred from the ADC and the measurements from Hγ.

5.8. Other Possible Explanations

In the previous subsections, we expounded our hypothesis that the observed difference between the molecular and ionized gas rotation velocities is due to eDIG in a thick disk with a vertical gradient in the rotation velocity. That is not, however, the only explanation. It is possible that we are instead measuring ionized gas velocities and velocity dispersions in the galactic bulge. To test this, we explore potential correlations between ΔV and the measured bulge-to-disk (B/D) luminosity ratios (Méndez-Abreu et al. 2017). Here, we use only results from the r-band because it overlaps with Hα. This
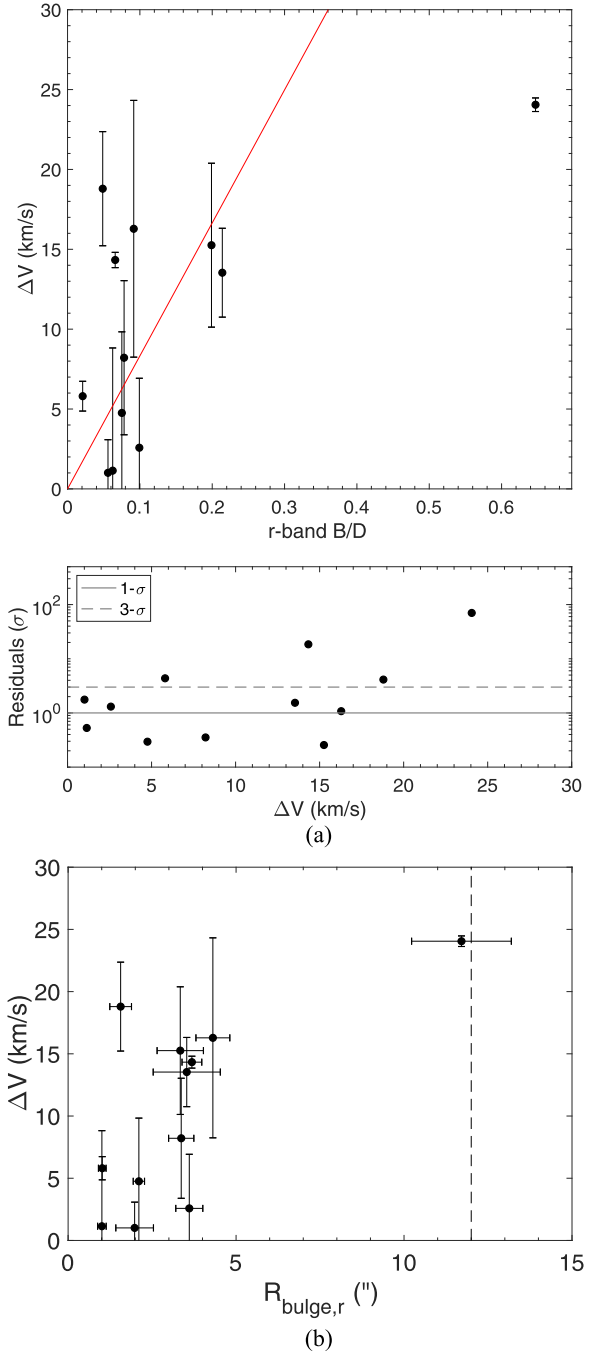
Figure 14. (a) The trend between the B/D ratio and ΔV. B/D ratios are derived from Méndez-Abreu et al. (2017), who do not report errors on those values. The red line is a linear fit to the data points, excluding NGC 2347, whose B/D ratio is an outlier compared to the other galaxies used here. The bottom panel shows the perpendicular distance from the line for each point in units of standard deviations plotted against ΔV. The solid and gray dashed lines show one- and three-sigma. For the r-band, 33% of the galaxies are consistent with the best-fit line within 1σ and 67% are consistent within 3σ. (b) We also investigate the relationship between the effective radius of the bulge (R_{bulge}) from Méndez-Abreu et al. (2017) and ΔV. All bulges (except NGC 2347) are much smaller than R_{2beam} (vertical dashed line), so contamination from the bulge is likely small in these galaxies.

is shown in the top panel of Figure 14(a). To determine whether there are any underlying correlations, we follow the same methodology as was used for the velocity dispersions discussed in Section 5.5.3. There is one galaxy, with a large B/

D ratio, that is a clear outlier from the rest; this galaxy is NGC 2347, which has the largest ΔV in the subsample. It is excluded from the fitting of the linear regression. The bottom panel of Figure 14(a) shows the distance of each galaxy from the best-fit line. For the r-band, 33% of galaxies are consistent with the best-fit line within 1σ, and 67% are consistent within 3σ. It is possible that the bulge could be affecting the measured rotation velocities and contributing to the measured ΔV. This affect is likely minimal, however, as ΔV is only measured at radii larger than $R_{2\mathrm{beam}}$ (12″, 4 kpc). Méndez-Abreu et al. (2017) also measure the effective bulge radius (R_{bulge}). We plot R_{bulge} versus ΔV in Figure 14(b). The dashed vertical line marks $R_{2\mathrm{beam}}$, which is the smallest radius included when measuring ΔV. Bulge contamination is likely for NGC 2347, because $R_{\mathrm{bulge}} \approx R_{2\mathrm{beam}}$, but the other galaxies in the sample have much smaller bulges, so the likelihood of contamination from the bulge is lessened. The exact contributions of the bulge and eDIG to ΔV are difficult to disentangle in detail, however, and it is likely that both contribute to the measured ΔV at some level.

6. Summary

We present a kinematic analysis of the EDGE-CALIFA survey, combining high-resolution CO maps from EDGE with CALIFA optical IFU data. Together, the CO and $H\alpha$ kinematics can be compared in a statistical sample. We summarize our results as follows, indicating the relevant figures and/or tables.

1. Using a sub-sample of 17 galaxies from the EDGE-CALIFA survey where precise molecular gas rotation curves could be derived, we fit CO and $H\alpha$ rotation curves, using the same geometric parameters, out to $\gtrsim 1R_e$ (Figure 18).

2. In our sub-sample, we find that most galaxies ($\sim$75%) have CO rotation velocities that are measurably higher than the $H\alpha$ rotation velocity in the outer part of the rotation curves. We refer to the median difference between the CO and $H\alpha$ rotation velocities as ΔV. Measurable differences between CO and $H\alpha$ rotation velocities range from 5 to 25 km s^{-1}, with a median value of 14 km s^{-1} (Figure 5).

3. The rotation velocity differences between CO and $H\alpha$ are not driven by inclination effects; we find no significant trend between the inclination and ΔV (Figure 8).

4. We suggest that these differences are caused by eDIG in these galaxies, which may constitute a thick, turbulent disk of ionized gas. Extraplanar ionized gas would be caused by stellar feedback, so we expect that galaxies with sufficient SFR per unit area (Σ_{SFR}) would have extended thick ionized gas disks and that galaxies with smaller Σ_{SFR} might have patchy extraplanar ionized gas above H II regions (Rand 1996; Rossa & Dettmar 2003a). Indeed, the majority of the galaxies in the high-quality rotation curve sub-sample ($\sim$95%) have sufficient Σ_{SFR} to harbor eDIG (Figure 9). Because EDGE galaxies were selected from CALIFA based on their FIR brightness (Bolatto et al. 2017), it is not surprising that the majority of them are star-forming disk galaxies with large Σ_{SFR}.

5. If galaxies frequently feature thick ionized gas disks, the effect described above would cause a systematic under-estimation of galaxy dynamical masses derived from ionized gas rotation velocity. Because we find that the ionized gas rotates more slowly than the molecular gas in galaxies with large Σ_{SFR}, this effect could be significant in local active star-forming galaxies, and even more so at higher redshifts, where SFRs are much higher on average.

6. We measure ionized gas velocity dispersion using the $H\gamma$ line ($\sigma_{H\gamma}$) as a proxy for $H\alpha$, and compare them to predictions for the ADC, assuming velocity dispersion explains the observed difference in rotation velocities (Figure 10). For the ADC, we infer velocity dispersion that would support a thick ionized gas disk with scale height ranging from $\sim$0.1–2.0 kpc. The velocity dispersion measured from the $H\gamma$ is comparable to, but somewhat smaller than, what we predicted from the ADC (Figure 11). The low spectral resolution of the data makes this measurement very difficult, so these results are tentative.

7. We find that [S II]/$H\alpha$ and [N II]/$H\alpha$, which are tracers of the WIM, are elevated in these galaxies compared to typical values in the plane of the MW ([S II]/$H\alpha = 0.11$, [N II]/$H\alpha \sim 0.25$; Madsen 2004; Madsen et al. 2006), but are not as large as typically found in the eDIG ([S II]/$H\alpha = 0.34$, [N II]/$H\alpha \gtrsim 0.5$; Madsen 2004; Blanc et al. 2009). This is likely because emission from the midplane and eDIG are mixed together in these measurements (Figure 12).

8. We investigate the effect of disk geometry by performing a suite of kinematic simulations with NEMO. We find that neither a thin disk nor a thick disk without a vertical gradient in the rotation velocity can reproduce the observed ΔV (Figures 13(a), (b)). The observed ΔV can be reproduced with a vertical gradient in rotation velocity. For a linear vertical rotation velocity gradient, our results favor $\eta \equiv 1 - \frac{V_{\mathrm{rot}}(z=h)}{V_0} \lesssim 0.3$ (Figure 13(c)). For a more realistic vertical rotation velocity gradient, our results can be reproduced with an eDIG scale height $\lesssim$1.5 kpc corresponding to a velocity dispersion $\lesssim$60 km s^{-1} (Figure 13(d)).

An ideal way to test for eDIG in these galaxies would be to directly measure the CO and $H\alpha$ scale heights in a sample of edge-on disks, and then correlate the $H\alpha$ scale height with ΔV. Additionally, a systematic decrease in the $H\alpha$ rotation velocity with distance from the midplane would be compelling evidence for our proposed model of a thick disk with a vertical velocity gradient. We plan to carry out this analysis using the edge-on galaxies in the EDGE-CALIFA survey in a forthcoming paper (R. C. Levy et al. 2018, in preparation).

Appendix A
Velocity Conventions

When converting from frequency (or wavelength) to a velocity via the Doppler formula, the radio and optical communities use different conventions as approximations to the full relativistic conversion. The optical convention is

$$\frac{V_{\text{opt}}}{c} = \frac{\lambda - \lambda_o}{\lambda_o} \equiv z, \tag{14}$$

the radio convention is

$$\frac{V_{\text{radio}}}{c} = \frac{\nu_o - \nu}{\nu_o} = \frac{z}{1+z}, \tag{15}$$

and the relativistic convention is

$$\frac{V_{\text{rel}}}{c} = \frac{\nu_o^2 - \nu^2}{\nu_o^2 + \nu^2}. \tag{16}$$

Therefore, combining Equations (14) and (15), a velocity measured in the optical convention (V_{opt}) can be converted to the radio convention (V_{radio}), where

$$V_{\text{radio}} = \frac{V_{\text{opt}}}{1 + \frac{V_{\text{opt}}}{c}}. \tag{17}$$

A galaxy with a rotation speed measured in the optical convention ($V_{\text{opt}}^{\text{rot}}$) will result in a radio rotation speed ($V_{\text{radio}}^{\text{rot}}$), where

$$V_{\text{radio}}^{\text{rot}} = \frac{V_{\text{opt}} + V_{\text{opt}}^{\text{rot}}}{1 + \frac{V_{\text{opt}} + V_{\text{opt}}^{\text{rot}}}{c}} - \frac{V_{\text{opt}}}{1 + \frac{V_{\text{opt}}}{c}} \approx \frac{V_{\text{opt}}^{\text{rot}}}{1 + \frac{2V_{\text{opt}}}{c}} \tag{18}$$

to first order. The rotation velocity in the optical convention is larger than in the radio convention. As an example, for a galaxy with $V_{\text{opt}} = 4500$ km s^{-1} and $V_{\text{opt}}^{\text{rot}} = 250$ km s^{-1} (similar to the

CALIFA galaxies), $V_{\text{radio}}^{\text{rot}} = 243$ km s^{-1}, so the rotation velocity in the radio convention is smaller than in the optical convention. For the velocity differences measured from the CO and Hα rotation curves, this discrepancy is not negligible. To avoid this, maps should be converted to the same convention.

Both the radio and optical convention scales become increasingly compressed at higher redshifts (large systemic velocities), but the relativistic convention does not suffer from this compression. Both EDGE and CALIFA reference to zero velocity, so typical velocities are a few thousand km s^{-1}. Conversions to the relativistic convention, from the radio or optical ones, were performed by combining Equation (15) or (14), respectively, with Equation (16), where

$$\frac{V_{\text{rel}}}{c} = \frac{\left(\frac{V_{\text{opt}}}{c} + 1\right)^2 - 1}{\left(\frac{V_{\text{opt}}}{c} + 1\right)^2 + 1} \tag{19}$$

and

$$\frac{V_{\text{rel}}}{c} = \frac{1 - \left(1 - \frac{V_{\text{radio}}}{c}\right)^2}{1 + \left(1 - \frac{V_{\text{radio}}}{c}\right)^2}. \tag{20}$$

For a rotational velocity measured in the relativistic frame ($V_{\text{rel}}^{\text{rot}}$), the corresponding $V_{\text{opt}}^{\text{rot}}$ and $V_{\text{radio}}^{\text{rot}}$ are

$$V_{\text{opt}}^{\text{rot}} = \frac{V_{\text{rel}}^{\text{rot}}}{1 - \frac{V_{\text{rel}}}{c}}, \tag{21}$$

$$V_{\text{radio}}^{\text{rot}} = \frac{V_{\text{rel}}^{\text{rot}}}{1 + \frac{V_{\text{rel}}}{c}}. \tag{22}$$

For a galaxy with $V_{\text{opt}} = 4500$ km s^{-1}, this results in $V_{\text{rel}} = 4466$ km s^{-1} (Equation (19)) and $V_{\text{radio}} = 4433$ km s^{-1} (Equation (17)). For a $V_{\text{opt}}^{\text{rot}} = 250$ km s^{-1}, this results in $V_{\text{rel}}^{\text{rot}} = 246$ km s^{-1} (Equation (21)) and $V_{\text{radio}}^{\text{rot}} = 242$ km s^{-1} (Equation (22)).

Therefore, to avoid the effects of different velocity conventions and compression, all EDGE and CALIFA velocity fields are converted to the relativistic convention using Equations (20) and (19), respectively. All velocities are reported in this convention unless otherwise noted.

Appendix B
Beam Smearing Correction

In order to accurately measure the CO and Hγ velocity dispersions, a beam smearing correction must be applied to the data cubes. As the beam size increases, rotation velocities from different radii can be blended into the linewidth. To correct for this effect, we fit a rotation-only model to the CO and Hα rotation curves and construct model rotation velocity fields. The smooth model rotation curve for each galaxy was constructed using the "universal rotation curve" (hereafter referred to as a Persic Profile) from Persic et al. (1996), which

Table 2
Parameters for the Persic Profile Fits

Name	CO $V(R_{opt})$ (km s^{-1})	CO L_B ($\times 10^8 L_{B\odot}$)	CO R_{opt} ($''$)	Hα $V(R_{opt})$ (km s^{-1})	Hα L_B ($\times 10^8 L_{B\odot}$)	Hα R_{opt} ($''$)
IC 1199	168.7	2.8	7.2	181.7	8.8	14.4
NGC 2253	145.9	1.7	6.3	146.6	2.0	10.5
NGC 2347	233.5	4.5	4.9	211.0	7.5	5.4
NGC 2410	198.8	2.5	10.9	175.1	9.8	4.3
NGC 3815	167.0	10.0	10.7	147.3	2.1	9.3
NGC 4047	174.8	10.0	6.4	177.9	10.0	10.1
NGC 4644	164.7	1.7	10.0	144.6	3.3	9.9
NGC 4711	131.1	9.4	12.6	138.4	10.0	16.1
NGC 5016	161.9	9.5	13.5	166.1	10.0	18.0
NGC 5480	90.7	9.9	6.7	110.3	10.0	18.6
NGC 5520	133.7	10.0	5.7	117.7	5.9	5.8
NGC 5633	165.2	10.0	11.3	148.4	2.9	9.6
NGC 5980	181.6	2.9	7.8	184.1	3.4	13.1
UGC 04132	199.8	10.0	10.7	207.2	10.0	15.5
UGC 05111	197.1	3.8	15.5	203.1	5.4	19.9
UGC 09067	185.8	2.1	8.0	169.9	7.4	7.7
UGC 10384	171.0	3.2	12.7	147.6	2.8	10.8

Note. $V(R_{opt})$, L_B, and R_{opt} for CO and Hα are the parameters from the Persic Profile fitting (Equation (23)).

is given by

$$
V_{Persic}(x) = V(R_{opt})\{[0.72 + 0.44\log(L_B/L_{B*})]
$$
$$
\times \frac{1.97x^{1.22}}{(x^2 + 0.78^2)^{1.43}} + 1.6\exp[-0.6(L_B/L_{B*})]
$$
$$
\times \frac{x^2}{x^2 + 1.5^2(L_B/L_{B*})^{0.4}}\}^{1/2} \text{ km s}^{-1},
$$
(23)

where $x = R/R_{opt}$. Persic et al. (1996) use $\log L_{B*} = 10.4$, where $L_{B*} = 6 \times 10^{10} h_{50}^{-2} L_{B\odot}$ (Persic & Salucci 1991) with $h = 0.75$; we also adopt this value of L_{B*}. R_{opt} is the optical radius. The Persic Profile was fit to V_{rot} using a nonlinear least squares fit with $V(R_{opt})$, L_B, and R_{opt} left as parameters to be fit, which are listed in Table 2. Model velocity fields were derived from the Persic Profile fits using a linear interpolation, then rotated and inclined based on the PA and inclination of the corresponding galaxy.

Using the rotation-only model velocity fields, we construct data cubes to simulate the effects of beam smearing. For the CO data, the channel width and spectral resolution are both 20 km s^{-1}. For each spaxel in the simulated CO data cube, a line is placed at the channel corresponding to the model rotation velocity of that pixel. The amplitude of the line is given by the value of the CO data cube at that voxel. The linewidth is a single 20 km s^{-1} channel. All other channels in that spaxel have zero amplitude. For the Hγ however, the channel width is 0.7 Å (48.4 km s^{-1}) and the spectral resolution (FWHM) is 2.3 Å (159.0 km s^{-1}). Therefore, at each spaxel in the simulated Hγ cube, a Gaussian line is placed at the channel corresponding to the model rotation velocity at that pixel. The FWHM of the Gaussian line is 2.3 Å. The amplitude of the line is given by the value of the Hγ data cube at that voxel. These simulated data cubes are then convolved to the corresponding CO or Hγ beam size using the convol task in Miriad. Model velocity dispersion maps (sigmas, not FWHM) are

created using the moment task in Miriad, which quantifies the velocity dispersion due to beam smearing. These model velocity dispersion maps are removed in quadrature from the corresponding CO or Hγ velocity dispersion maps, yielding a beam smearing corrected velocity dispersion map. Because the simulated data cubes incorporate the instrumental linewidth, removing the simulated velocity dispersion map also corrects for the instrumental linewidth. The beam smearing corrected velocity dispersion maps are then masked to the same region where ΔV is calculated, which excludes the centers where the beam smearing corrections are large. Figure 15 shows the stages of the beam smearing correction for both CO (a) and Hγ (b) for NGC 2347. We note that, after this masking, the difference between the beam smearing correction applied here and simply removing the instrumental linewidth in quadrature is $\sim$2 km s^{-1} over the whole KSS sample. Each CO and Hγ velocity dispersion map has a corresponding error map. The weighted average CO or Hγ velocity dispersion for each galaxy is

$$
\langle\sigma\rangle = \frac{\Sigma(\sigma_i/\delta_{\sigma_i}^2)}{\Sigma(1/\delta_{\sigma_i}^2)},
$$
(24)

where σ_i is the velocity dispersion and $\delta_{\sigma i}$ is the error on the velocity dispersion at each pixel. The error on $\langle\sigma\rangle$ is the weighted standard deviation given by

$$
\sigma_{\langle\sigma\rangle} = \sqrt{\frac{N}{\Sigma(1/\delta_{\sigma_i}^2)}}.
$$
(25)

The resulting beam smearing corrected average CO and Hγ velocity dispersions are listed in Table 1. A comparison of the CO and Hγ velocity dispersions is shown in Figure 16 for the KSS galaxies. We note that previous measurements of CO velocity dispersions from HERACLES in bright GMCs are $\sim$7 km s^{-1}, but increase to $\sim$12 km s^{-1} if a larger beam that encompasses more diffuse CO is used (Mogotsi et al. 2016). The EDGE data are at $\sim$kpc resolution and would encompass
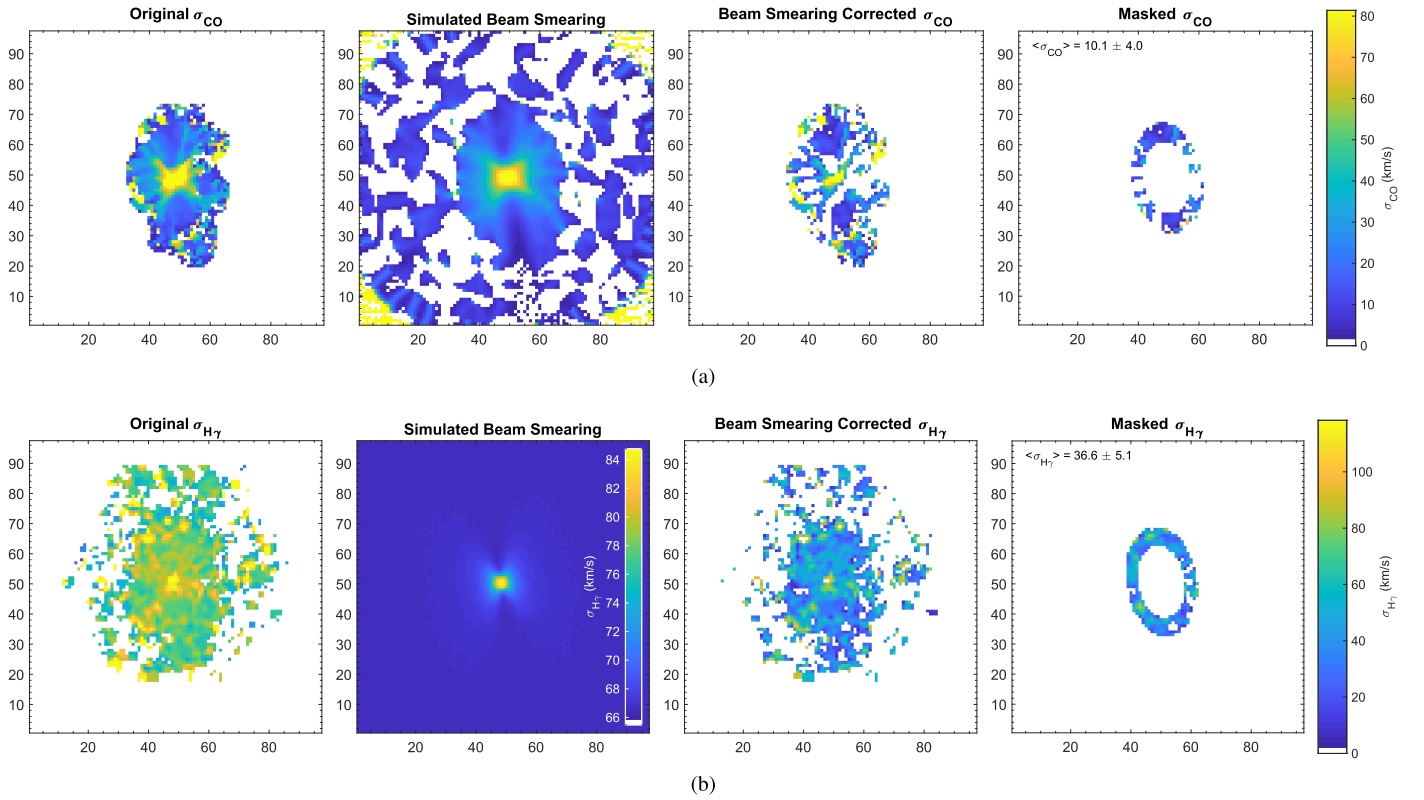
Figure 15. The progression of the beam smearing correction for (a) CO and (b) Hγ for NGC 2347. From left to right, the panels show the original velocity dispersion map, the simulated velocity dispersion due to beam smearing, the beam smearing corrected velocity dispersion, and the masked beam smearing corrected velocity dispersion. All panels are normalized to the color scales shown to the right, except for the Hγ simulated beam smearing, whose color scale is shown in the inset. White patches in the right two columns are where the simulated beam smearing is larger than the original velocity dispersion and are imaginary when removed in quadrature. These points are discarded for the analysis.
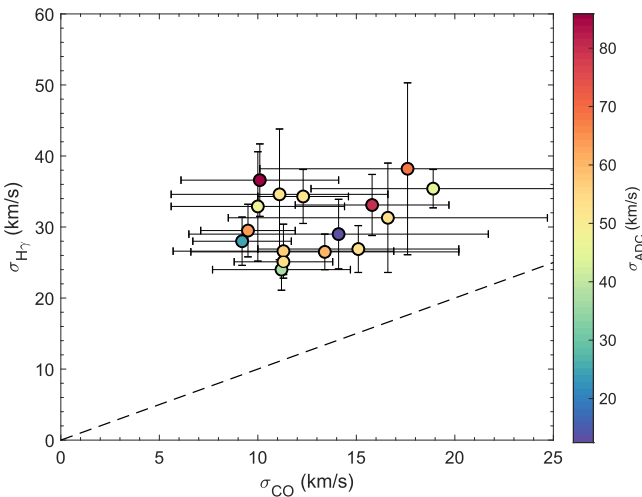
Figure 16. The beam smearing corrected CO and Hγ velocity dispersions for the KSS galaxies. Points are color-coded by the velocity dispersion inferred from the ADC. The dashed line is one-to-one.

diffuse CO as well as denser GMCs, and the values we derive are consistent with these results.

Appendix C
Galaxy-by-galaxy Data, Figures, and Descriptions

Kinematic parameters used for the EDGE and CALIFA data for all 126 galaxies are listed in Tables 3 and 4, respectively. If

kinematic parameters could not be fit, values were taken from outer isophote photometry (Falcón-Barroso et al. 2017) or from HyperLeda. Previous work to determine kinematic PAs in a subset of the CALIFA galaxies has also been carried out by García-Lorenzo et al. (2015) and Barrera-Ballesteros et al. (2014, 2015). More details are in the table captions. The lack of trends with global parameters, discussed in Section 5.3, are shown in Figure 17. CO and Hα velocity fields and rotation curves are shown for each galaxy in the KSS in Figure 18. We provide brief comments on each galaxy in the KSS.

IC 1199—This galaxy's CO velocity field is somewhat patchy due to the SN masking; however, its CO rotation curve is excellent, having radial and systemic components near zero. The Hα rotation curve is interesting, as it flattens until ∼13″ then rises to meet the CO rotation curve. The Hα rotation curve generally has small radial and systemic components, although there is some non-zero radial component where the Hα rotation curve flattens, which may explain the disagreement between the CO and Hα rotation curves in this region. The Hα systemic velocity is non-zero in the center, but this will not affect the results because that region is excluded. Neither the H I W50 nor W90 agree well with the CO or Hα rotation curves.

NGC 2253—This galaxy's CO rotation curve is excellent, although there is a small trend in the radial component over the region of comparison. Its Hα rotation curve has large radial and systemic components in the center, but they are near zero over the comparison region. The CO and Hα rotation components cross, and the CO V_{rot} continues to rise despite the flattened Hα. Both the H I W50 and W90 are larger than the CO and Hα V_{rot}.

Table 3
Geometric Parameters for the EDGE Data

Name	R.A. (J2000)	Decl. (J2000)	PA (°)	Inc (°)	$V_{\rm sys}$ (km s^{-1})	$X_{\rm off}$ ('')	$Y_{\rm off}$ ('')	PA Flag	Inc Flag	$V_{\rm sys}$ Flag
ARP 220	233.73900	23.50270	337.7	29.7	5247	0.0	0.0	P	P	C
IC 0480	118.84665	26.74280	167.9	76.6	4595	0.0	0.0	P	P	C
IC 0540	142.54290	7.90259	350.0	68.3	2022	0.0	0.0	P	P	C
IC 0944	207.87900	14.09200	105.7	75.0	6907	0.0	0.0	P	C	C
IC 1151	239.63550	17.44150	203.9	68.0	2192	0.0	0.0	C	P	C
IC 1199	242.64300	10.04010	339.3	64.5	4686	0.6	1.1	C	P	C
IC 1683	20.66190	34.43700	15.6	54.8	4820	0.0	0.0	P	C	C
IC 2247	123.99615	23.19960	328.5	77.7	4254	0.0	0.0	P	P	C
IC 2487	142.53840	20.09090	162.9	77.9	4310	0.0	0.0	P	P	C
IC 4566	234.17550	43.53940	145.0	53.9	5537	0.0	0.0	C	P	C
IC 5376	0.33233	34.52570	3.4	71.6	4979	0.0	0.0	P	P	C
NGC 0444	18.95685	31.08020	158.7	74.9	4776	0.0	0.0	P	P	H
NGC 0447	18.90660	33.06760	227.0	29.1	5552	0.8	0.8	C	P	C
NGC 0477	20.33475	40.48820	140.0	60.0	5796	0.0	0.0	C	P	C
NGC 0496	20.79810	33.52890	36.5	57.0	5958	−0.4	1.6	C	P	C
NGC 0523	21.33660	34.02500	277.2	71.6	4760	0.0	0.0	C	P	C
NGC 0528	21.38985	33.67150	57.7	61.1	4638	−3.0	1.8	P	P	H
NGC 0551	21.91935	37.18290	315.0	64.2	5141	0.0	0.0	C	P	C
NGC 1167	45.42660	35.20570	87.5	39.5	4797	−6.5	3.5	C	P	C
NGC 2253	100.92420	65.20620	300.0	47.4	3545	0.0	0.0	C	P	C
NGC 2347	109.01625	64.71080	189.1	50.2	4387	2.5	1.9	P	P	C
NGC 2410	113.75940	32.82210	216.6	71.6	4642	0.0	0.0	C	P	C
NGC 2480	119.29350	23.77980	343.1	55.4	2287	0.0	0.0	C	P	C
NGC 2486	119.48535	25.16080	92.9	55.6	4569	0.0	0.0	P	P	H
NGC 2487	119.58540	25.14920	117.5	31.4	4795	0.0	0.0	C	P	C
NGC 2623	129.60000	25.75410	255.0	45.6	5454	0.0	0.0	C	P	C
NGC 2639	130.90845	50.20540	314.3	49.5	3162	−1.4	0.6	C	P	C
NGC 2730	135.56580	16.83830	260.8	27.7	3802	0.0	0.0	P	P	C
NGC 2880	142.39410	62.49060	322.9	49.9	1530	0.0	0.0	P	P	H
NGC 2906	143.02605	8.44159	262.0	55.7	2133	0.0	0.0	C	P	C
NGC 2916	143.73990	21.70520	199.9	49.9	3620	0.0	0.0	P	P	C
NGC 2918	143.93355	31.70550	75.1	46.1	6569	0.0	0.0	P	P	H
NGC 3303	159.25050	18.13570	159.6	60.5	6040	0.0	0.0	P	P	H
NGC 3381	162.10350	34.71140	333.1	30.8	1625	0.0	0.0	C	P	H
NGC 3687	172.00200	29.51100	326.0	19.6	2497	0.0	0.0	C	P	H
NGC 3811	175.32000	47.69080	351.5	39.9	3073	−2.6	0.1	P	P	C
NGC 3815	175.41300	24.80040	67.8	59.9	3686	3.0	0.1	P	P	C
NGC 3994	179.40300	32.27730	188.1	59.5	3097	2.4	1.6	P	P	C
NGC 4047	180.71100	48.63620	104.0	42.1	3419	0.5	0.0	C	P	C
NGC 4149	182.63700	58.30410	85.0	66.2	3050	−0.5	−0.9	C	P	C
NGC 4185	183.34200	28.51100	344.4	48.2	3874	0.0	0.0	P	P	C
NGC 4210	183.81600	65.98540	277.7	40.9	2714	0.0	0.0	P	P	C
NGC 4211NED02	183.90600	28.16960	25.0	30.0	6605	0.0	0.0	C	C	C
NGC 4470	187.40700	7.82390	349.5	47.5	2338	0.0	0.0	C	P	C
NGC 4644	190.67850	55.14550	57.0	72.9	4915	−3.2	−0.1	P	P	C
NGC 4676A	191.54250	30.73210	185.3	50.0	6541	−2.1	−0.8	C	C	C
NGC 4711	192.19050	35.33270	220.0	58.3	4044	3.0	0.6	C	P	C
NGC 4961	196.44900	27.73390	100.0	46.6	2521	−2.2	0.4	C	P	C
NGC 5000	197.44800	28.90680	31.3	20.0	5557	0.0	0.0	C	C	C
NGC 5016	198.02850	24.09500	57.4	39.9	2588	−0.1	−0.6	P	P	C
NGC 5056	199.05150	30.95020	178.0	61.4	5544	−1.0	1.0	C	L	C
NGC 5205	202.51500	62.51150	169.0	49.8	1762	0.0	0.0	P	P	C
NGC 5218	203.04300	62.76780	236.4	30.1	2888	0.0	0.0	C	P	C
NGC 5394	209.64000	37.45350	189.3	70.2	3431	0.0	0.0	C	P	C
NGC 5406	210.08400	38.91540	111.4	45.0	5350	0.0	0.0	P	P	C
NGC 5480	211.59000	50.72510	183.0	41.5	1879	−0.9	−0.4	C	L	C
NGC 5485	211.79700	55.00160	74.5	47.2	1893	2.0	−0.6	C	P	H
NGC 5520	213.09450	50.34850	245.1	59.1	1870	1.1	0.4	C	P	C
NGC 5614	216.03150	34.85890	270.0	35.9	3859	0.0	0.0	C	P	C
NGC 5633	216.86850	46.14640	16.9	41.9	2319	0.0	0.0	P	P	C
NGC 5657	217.68150	29.18070	349.0	68.3	3860	2.1	0.2	C	P	C
NGC 5682	218.68800	48.66950	310.6	76.3	2242	−0.9	1.7	C	P	H
NGC 5732	220.16250	38.63770	43.2	58.4	3723	−2.0	−0.2	P	P	C
NGC 5784	223.56900	42.55780	255.0	45.0	5427	−2.1	0.6	C	C	C
NGC 5876	227.38200	54.50650	51.4	65.9	3240	−0.1	0.6	P	P	H
NGC 5908	229.18050	55.40940	153.0	77.0	3294	0.0	0.0	C	C	C

Table 3
(Continued)

Name	R.A. (J2000)	Decl. (J2000)	PA (°)	Inc (°)	V_{sys} (km s^{-1})	X_{off} ($''$)	Y_{off} ($''$)	PA Flag	Inc Flag	V_{sys} Flag
NGC 5930	231.53250	41.67610	155.0	45.0	2637	2.2	0.1	C	C	C
NGC 5934	232.05300	42.92990	5.0	55.0	5566	0.0	0.0	C	C	C
NGC 5947	232.65300	42.71720	248.6	32.2	5898	−0.9	0.1	C	P	C
NGC 5953	233.63550	15.19380	48.3	26.0	1988	−1.0	0.4	C	C	C
NGC 5980	235.37700	15.78760	15.0	66.2	4060	−1.0	1.0	L	P	C
NGC 6004	237.59400	18.93920	272.3	37.3	3818	3.2	1.1	C	P	C
NGC 6021	239.37750	15.95600	157.1	43.4	4673	1.7	−0.1	P	P	H
NGC 6027	239.80200	20.76330	231.4	30.9	4338	0.0	0.0	P	P	H
NGC 6060	241.46700	21.48490	102.0	64.3	4416	−1.2	−0.2	P	P	C
NGC 6063	241.80450	7.97887	331.6	56.2	2807	0.0	0.0	C	P	H
NGC 6081	243.23700	9.86703	308.2	65.6	4978	0.0	0.0	P	P	H
NGC 6125	244.79850	57.98410	4.8	16.9	4522	0.0	0.0	P	P	H
NGC 6146	246.29250	40.89260	78.3	40.7	8693	0.0	0.0	C	P	H
NGC 6155	246.53400	48.36680	130.0	44.7	2418	3.0	3.0	C	P	C
NGC 6168	247.83750	20.18550	111.1	76.6	2540	0.0	0.0	L	P	C
NGC 6186	248.60700	21.54090	64.6	71.2	2940	−3.0	0.5	C	L	C
NGC 6301	257.13600	42.33900	288.5	52.8	8222	0.0	0.0	P	P	C
NGC 6310	256.98900	60.99010	69.9	73.7	3459	0.0	0.0	P	P	C
NGC 6314	258.16200	23.27020	356.0	57.7	6551	−2.2	0.0	C	P	C
NGC 6361	259.67100	60.60810	46.8	75.0	3791	0.0	0.0	C	C	C
NGC 6394	262.59000	59.63990	237.4	60.0	8453	0.0	0.0	C	C	C
NGC 6478	267.15900	51.15720	29.2	73.4	6756	0.0	0.0	C	C	C
NGC 7738	356.00850	0.51671	234.7	65.6	6682	0.0	0.0	C	P	C
NGC 7819	1.10206	31.47200	270.3	54.0	4918	0.0	0.0	C	P	C
UGC 00809	18.96615	33.81070	18.6	78.9	4171	0.0	0.0	C	P	C
UGC 03253	79.92345	84.05250	267.7	58.3	4040	0.0	0.0	P	P	H
UGC 03539	102.22470	66.26130	302.9	72.1	3278	0.0	0.0	C	P	C
UGC 03969	115.30965	27.61410	134.3	70.0	8029	0.0	0.0	P	C	C
UGC 03973	115.63560	49.80980	143.8	39.1	6594	0.5	−1.8	C	P	C
UGC 04029	117.07920	34.33220	63.5	77.6	4389	0.0	0.0	C	P	C
UGC 04132	119.80425	32.91490	212.6	72.0	5151	0.0	−0.8	C	P	C
UGC 04280	123.63885	54.79950	183.7	71.5	3500	0.0	0.0	P	P	C
UGC 04461	128.34450	52.53230	222.8	70.1	4941	0.0	0.0	C	P	C
UGC 05108	143.85960	29.81260	136.1	66.1	8015	0.0	0.0	C	P	C
UGC 05111	144.21855	66.78840	118.3	72.9	6660	2.0	−1.0	C	P	C
UGC 05244	147.20070	64.16800	32.8	77.9	2974	0.0	0.0	P	P	H
UGC 05359	149.71530	19.21500	94.5	72.3	8344	−0.9	0.8	C	P	C
UGC 05498NED01	153.01500	23.08540	61.8	81.0	6250	0.0	0.0	C	C	H
UGC 05598	155.55900	20.58940	215.6	74.8	5591	0.0	0.0	P	P	C
UGC 06312	169.50000	7.84466	224.6	68.7	6266	0.0	0.0	C	P	H
UGC 07012	180.51300	29.84810	184.1	60.5	3052	0.0	0.0	C	P	H
UGC 08107	194.91600	53.34130	228.2	71.4	8201	0.0	0.0	C	P	C
UGC 08250	197.58450	32.48260	11.7	76.2	5169	0.0	0.0	C	P	H
UGC 08267	197.79750	43.72650	223.0	75.4	7159	−1.0	0.0	C	P	C
UGC 09067	212.68950	15.20920	14.6	62.4	7740	0.0	0.0	C	P	C
UGC 09476	220.38300	44.51270	307.0	48.5	3243	0.0	0.0	C	P	C
UGC 09537	222.11100	34.99800	135.7	72.0	8662	0.0	0.0	C	C	C
UGC 09542	222.25500	42.46400	214.3	72.7	5417	2.1	−1.9	P	P	C
UGC 09665	225.38550	48.31980	138.2	74.0	2561	0.0	0.0	P	P	C
UGC 09759	227.67000	55.35040	49.7	66.8	3394	3.6	−2.1	P	P	C
UGC 09873	232.46100	42.62900	129.0	75.3	5575	0.0	0.0	C	P	C
UGC 09892	233.21700	41.19140	101.0	72.2	5591	0.0	0.0	P	P	C
UGC 09919	233.91450	12.60630	349.2	77.9	3160	0.0	0.0	P	P	C
UGC 10043	237.17250	21.86950	327.8	90.0	2154	−2.4	−0.6	C	L	C
UGC 10123	239.76150	51.30460	231.6	70.0	3738	3.6	−0.4	C	C	C
UGC 10205	241.66800	30.09900	128.6	51.7	6491	0.0	0.0	C	P	C
UGC 10331	244.33800	59.32010	140.8	76.2	4415	0.0	0.0	P	P	H
UGC 10380	246.45750	16.57610	288.2	77.9	8624	0.0	0.0	P	P	C
UGC 10384	246.69450	11.58020	275.8	70.0	4927	0.0	0.0	C	C	C
UGC 10710	256.71900	43.12210	329.5	69.6	8228	0.0	0.0	L	P	C

Note. The table lists the geometric parameters used for the EDGE data for each galaxy. R.A. and decl. values are taken from Bolatto et al. (2017). The V_{sys} values are reported in the relativistic convention. PA Flag, Inc Flag, and V_{sys} Flag indicate whether those respective values were derived from CO kinematic fits (C) or Hα kinematic fits (H) done in this work, from photometric fits to the outer isophotes (P) (Falcón-Barroso et al. 2017), or from HyperLeda (L).

Table 4
Geometric Parameters for the CALIFA Data

Name	R_e (″)	V500 V_{sys} (km s^{-1})	V500 X_{off} (″)	V500 Y_{off} (″)	V1200 V_{sys} (km s^{-1})	V1200 X_{off} (″)	V1200 Y_{off} (″)
ARP 220	12.7	5294	0.0	0.0	5247	0.0	0.0
IC 0480	11.5	4553	0.0	0.0	4518	0.0	0.0
IC 0540	14.9	2050	0.0	0.0	2043	0.0	0.0
IC 0944	9.8	6854	0.2	2.5	6805	−2.5	3.4
IC 1151	19.3	2122	0.0	0.0	2114	0.0	0.0
IC 1199	18.8	4636	0.0	2.5	4625	0.3	3.0
IC 1683	10.0	4787	−3.4	1.4	4704	−3.0	3.4
IC 2247	16.3	4218	0.4	0.6	4188	0.0	0.0
IC 2487	16.8	4281	0.0	0.0	4250	0.0	0.0
IC 4566	13.2	5504	1.2	0.1	5453	1.2	0.1
IC 5376	11.6	4944	0.0	0.0	4903	0.0	0.0
NGC 0444	17.4	4776	−4.0	2.6	4738	−4.0	2.6
NGC 0447	18.6	5489	0.8	0.8	5439	0.8	0.8
NGC 0477	18.6	5794	0.0	0.0	5738	0.0	0.0
NGC 0496	16.5	5966	−3.0	3.0	5898	0.4	2.1
NGC 0523	8.1	4719	0.0	0.0	4682	0.0	0.0
NGC 0528	9.0	4638	−3.7	0.7	4602	−3.7	0.7
NGC 0551	14.4	5106	0.0	0.0	5091	−0.9	1.6
NGC 1167	21.6	4875	−6.6	2.3	4835	−6.6	2.3
NGC 2253	4.1	3530	2.4	0.6	3540	1.1	2.1
NGC 2347	13.8	4383	3.6	3.3	4373	1.9	3.6
NGC 2410	17.9	4650	1.6	2.6	4648	0.9	0.9
NGC 2480	10.8	2305	0.0	0.0	2296	0.0	0.0
NGC 2486	13.0	4569	0.0	0.0	4534	0.0	0.0
NGC 2487	18.8	4808	0.0	0.0	4769	0.0	0.0
NGC 2623	11.9	5440	2.5	0.5	5391	2.5	0.5
NGC 2639	13.4	3157	−1.1	−2.6	3142	1.9	2.3
NGC 2730	14.6	3773	0.0	0.0	3749	0.0	0.0
NGC 2880	13.7	1530	0.0	0.0	1526	0.0	0.0
NGC 2906	15.2	2142	1.6	0.5	2140	−0.1	2.1
NGC 2916	20.6	3664	0.0	0.0	3642	0.0	0.0
NGC 2918	9.3	6569	−0.6	2.4	6497	−0.6	2.4
NGC 3303	9.2	6040	0.0	0.0	5979	0.0	0.0
NGC 3381	14.8	1625	0.0	0.0	1621	0.0	0.0
NGC 3687	15.4	2497	3.2	0.1	2487	3.2	0.1
NGC 3811	14.7	3061	−2.6	0.1	3071	−1.0	0.0
NGC 3815	8.8	3690	3.0	0.1	3648	1.6	2.1
NGC 3994	7.1	3089	3.2	1.0	3055	1.6	1.5
NGC 4047	14.8	3376	1.2	−0.7	3396	0.9	2.0
NGC 4149	11.5	3042	−0.5	−0.9	3027	−0.5	−0.9
NGC 4185	22.6	3831	0.0	0.0	3807	0.0	0.0
NGC 4210	16.9	2689	2.6	3.1	2687	−1.4	2.1
NGC 4211NED02	14.0	6555	0.0	0.0	6483	0.0	0.0
NGC 4470	11.5	2319	3.2	0.5	2310	3.2	0.5
NGC 4644	14.3	4889	−1.2	0.0	4885	−2.9	−0.9
NGC 4676A	13.5	6518	−2.1	−0.8	6447	−2.1	−0.8
NGC 4711	12.3	4044	4.0	0.8	4007	2.5	0.0
NGC 4961	9.7	2528	−2.2	0.4	2517	−2.2	0.4
NGC 5000	10.2	5505	0.0	0.0	5454	0.0	0.0
NGC 5016	15.3	2539	−0.1	−0.6	2586	−1.9	0.5
NGC 5056	13.8	5530	−1.5	1.0	5453	−0.4	0.9
NGC 5205	16.4	1743	0.0	0.0	1738	0.0	0.0
NGC 5218	12.3	2855	0.0	0.0	2841	0.0	0.0
NGC 5394	16.8	3404	0.0	0.0	3385	0.0	0.0
NGC 5406	14.9	5313	0.0	0.0	5331	−0.8	0.9
NGC 5480	17.4	1851	−0.9	−2.5	1908	−3.5	−0.3
NGC 5485	21.8	1893	2.0	−0.6	1887	2.0	−0.6
NGC 5520	11.9	1852	3.0	0.0	1893	1.8	1.1
NGC 5614	15.7	3824	3.4	−0.6	3800	3.4	−0.6
NGC 5633	12.9	2295	0.0	1.5	2290	3.1	1.8
NGC 5657	11.6	3861	3.1	−0.5	3836	3.1	−0.5
NGC 5682	19.6	2242	0.0	1.1	2234	0.0	1.1
NGC 5732	12.3	3703	−1.0	−0.6	3680	−1.0	−0.6
NGC 5784	11.9	5420	−0.4	2.5	5307	−2.4	−0.4
NGC 5876	15.1	3240	1.0	0.5	3222	1.0	0.5
NGC 5908	14.6	3258	1.0	−0.3	3240	1.0	−0.3

Table 4
(Continued)

Name	R_e ($''$)	V500 V_{sys} (km s^{-1})	V500 X_{off} ($''$)	V500 Y_{off} ($''$)	V1200 V_{sys} (km s^{-1})	V1200 X_{off} ($''$)	V1200 Y_{off} ($''$)
NGC 5930	14.4	2590	3.4	−0.1	2579	3.4	−0.1
NGC 5934	6.7	5556	2.5	−1.2	5505	2.5	−1.2
NGC 5947	10.5	5863	−3.2	2.4	5811	−3.2	−0.1
NGC 5953	9.1	1967	0.1	0.0	1961	0.1	0.0
NGC 5980	12.6	4049	0.0	2.0	4021	−0.9	0.3
NGC 6004	20.4	3781	4.4	0.8	3757	4.4	0.8
NGC 6021	8.5	4673	2.6	−0.4	4637	2.6	−0.4
NGC 6027	10.8	4338	0.0	0.0	4307	0.0	0.0
NGC 6060	20.2	4337	0.0	0.0	4306	0.0	0.0
NGC 6063	17.8	2807	0.0	0.0	2794	0.0	0.0
NGC 6081	10.4	4978	0.0	0.0	4937	0.0	0.0
NGC 6125	15.4	4522	0.0	0.0	4488	0.0	0.0
NGC 6146	11.0	8693	0.0	0.0	8567	0.0	0.0
NGC 6155	13.5	2381	4.0	1.0	2396	−1.4	0.4
NGC 6168	16.3	2505	0.0	0.0	2495	0.0	0.0
NGC 6186	12.7	2910	−3.0	0.5	2896	−3.0	0.5
NGC 6301	20.0	8221	3.5	−0.8	8118	2.0	−0.5
NGC 6310	15.8	3377	0.0	0.0	3358	0.0	0.0
NGC 6314	8.7	6493	−2.2	0.0	6423	−2.2	0.0
NGC 6361	15.4	3759	0.0	0.0	3714	3.3	−2.4
NGC 6394	9.0	8387	0.0	0.0	8261	−0.6	0.5
NGC 6478	17.4	6735	0.0	0.0	6659	0.0	0.0
NGC 7738	11.5	6642	0.0	0.0	6568	0.0	0.0
NGC 7819	15.0	4898	0.0	0.0	4858	0.0	0.0
UGC 00809	11.0	4143	−3.0	1.0	4114	0.0	0.0
UGC 03253	12.7	4040	0.0	0.0	4013	0.0	0.0
UGC 03539	13.7	3244	2.8	4.6	3250	−1.4	3.3
UGC 03969	11.2	8001	0.0	0.0	7896	−2.4	−0.5
UGC 03973	9.9	6551	0.5	−1.8	6479	0.5	−1.8
UGC 04029	15.0	4367	0.0	0.0	4335	0.0	0.0
UGC 04132	13.2	5158	0.0	0.0	5105	0.2	0.6
UGC 04280	11.2	3485	0.0	0.0	3465	0.0	0.0
UGC 04461	11.9	4954	0.0	0.0	4913	0.0	0.0
UGC 05108	9.6	7987	−1.0	1.0	7881	0.0	0.0
UGC 05111	12.7	6657	0.0	0.0	6557	3.4	−1.3
UGC 05244	12.6	2974	−0.5	−5.0	2959	−2.0	−4.0
UGC 05359	12.4	8332	0.0	0.0	8226	−0.4	1.5
UGC 05498NED01	10.5	6250	0.0	0.0	6185	0.0	0.0
UGC 05598	11.4	5601	0.0	0.0	5549	0.0	0.0
UGC 06312	12.8	6266	0.0	0.0	6201	0.0	0.0
UGC 07012	11.9	3052	0.0	0.0	3036	0.0	0.0
UGC 08107	17.7	8199	0.0	0.0	8139	−0.4	2.5
UGC 08250	11.8	5169	0.0	0.0	5124	0.0	0.0
UGC 08267	10.5	7102	−0.4	0.3	7018	−0.4	0.3
UGC 09067	11.3	7733	0.1	1.1	7661	1.0	0.0
UGC 09476	15.5	3201	0.0	0.0	3184	0.0	0.0
UGC 09537	15.8	8653	0.0	0.0	8528	0.0	0.0
UGC 09542	12.9	5399	1.2	−0.4	5350	1.2	−0.4
UGC 09665	11.6	2511	0.0	0.0	2500	0.0	0.0
UGC 09759	13.5	3397	3.6	−2.1	3378	3.6	−2.1
UGC 09873	14.8	5533	0.0	0.0	5482	0.0	0.0
UGC 09892	13.7	5582	0.0	0.0	5530	0.0	0.0
UGC 09919	13.1	3167	0.0	0.0	3150	0.0	0.0
UGC 10043	24.6	2128	−0.5	−1.0	2120	−1.5	−1.0
UGC 10123	11.0	3701	4.8	−0.5	3709	3.6	−0.4
UGC 10205	14.0	6445	0.0	0.0	6376	0.0	0.0
UGC 10331	15.4	4415	0.0	0.0	4382	0.0	0.0
UGC 10380	12.8	8592	0.0	0.0	8469	0.0	0.0
UGC 10384	9.3	4891	−0.8	0.3	4886	0.4	−0.6
UGC 10710	12.0	8184	0.2	−0.2	8072	0.2	−0.2

Note. The table lists those geometric parameters used for the CALIFA data for each galaxy that are not already reported in Table 3. The R_e values, provided by the CALIFA team, are derived from growth curves fit to SDSS r-band images (Sánchez et al. 2014). V500 parameters were determined from kinematic fits to Hα, and V1200 parameters were determined from kinematic fits to Hγ. The V_{sys} values are reported in the relativistic convention.
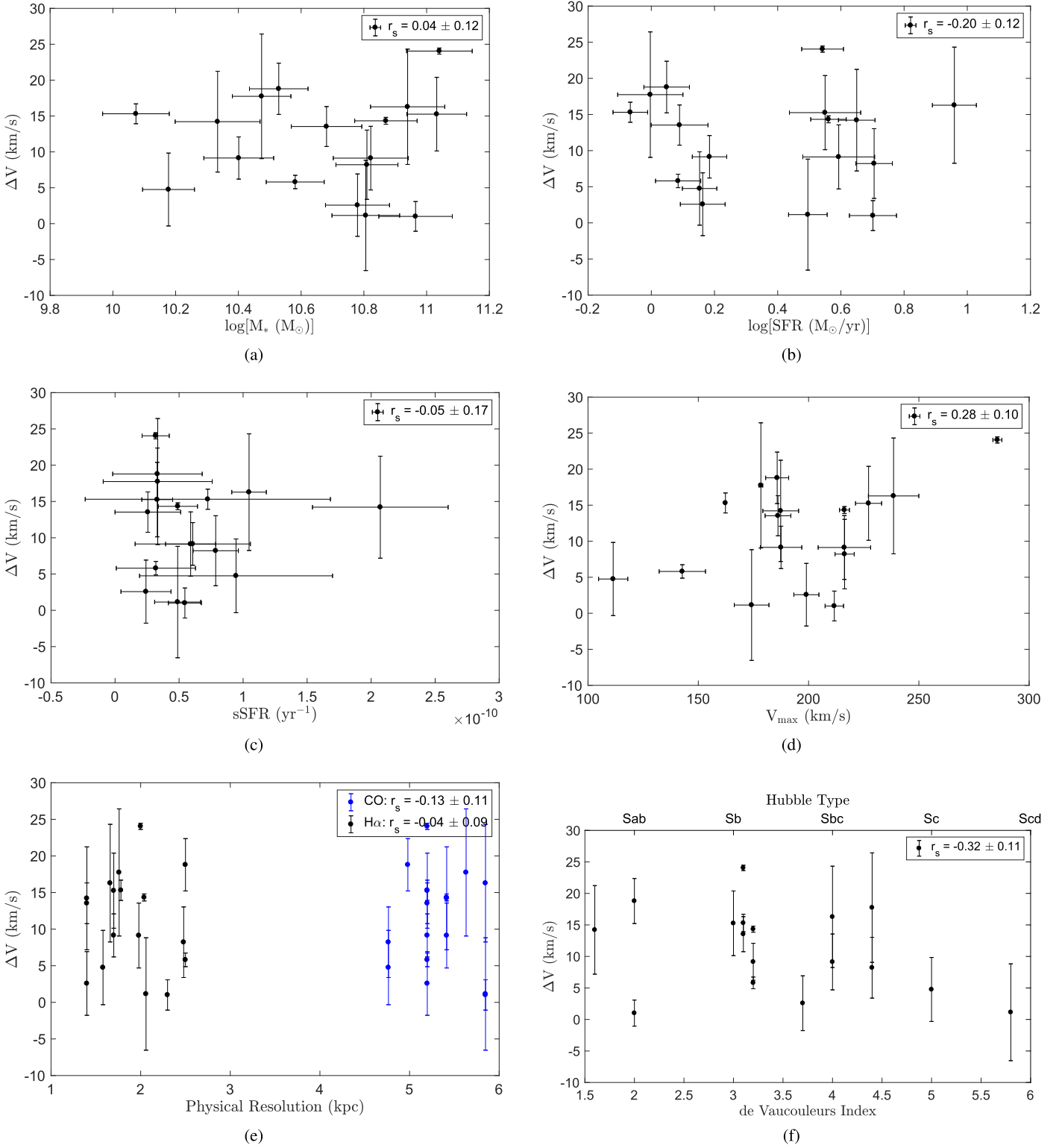
Figure 17. There are no trends between ΔV and (a) M_*, (b) SFR, (c) sSFR, (d) CO V_{max}, (e) physical resolution of the native (unconvolved) CO (blue) and Hα (black) data, and (f) morphology. The Spearman rank correlation coefficients (r_s) are shown in the top right of each panel. de Vaucouleurs indexes are taken from HyperLeda. The lack of trend with physical resolution justifies our choice to convolve to a common angular resolution rather than to a common physical resolution.

NGC 2347—This galaxy is used as an example throughout this work. Overall, its CO and Hα rotation curves are excellent. The ΔV is large; much greater than the errors on the rotation curves. Although there is a bump in the CO radial component in the comparison region, it likely cannot account for the ΔV. The H I W50 and W90 straddle the CO V_{rot}, potentially

indicating that the Hα scale height in this galaxy is larger than the H I, which is closer to the CO scale height. This galaxy has a reported ring structure (Bolatto et al. 2017). It is also potentially an AGN candidate, based on its [O III]/Hβ and [N II]/Hα ratios. However, because the central 12″ ($\sim$4 kpc) are excluded from analysis, any AGN contamination should be
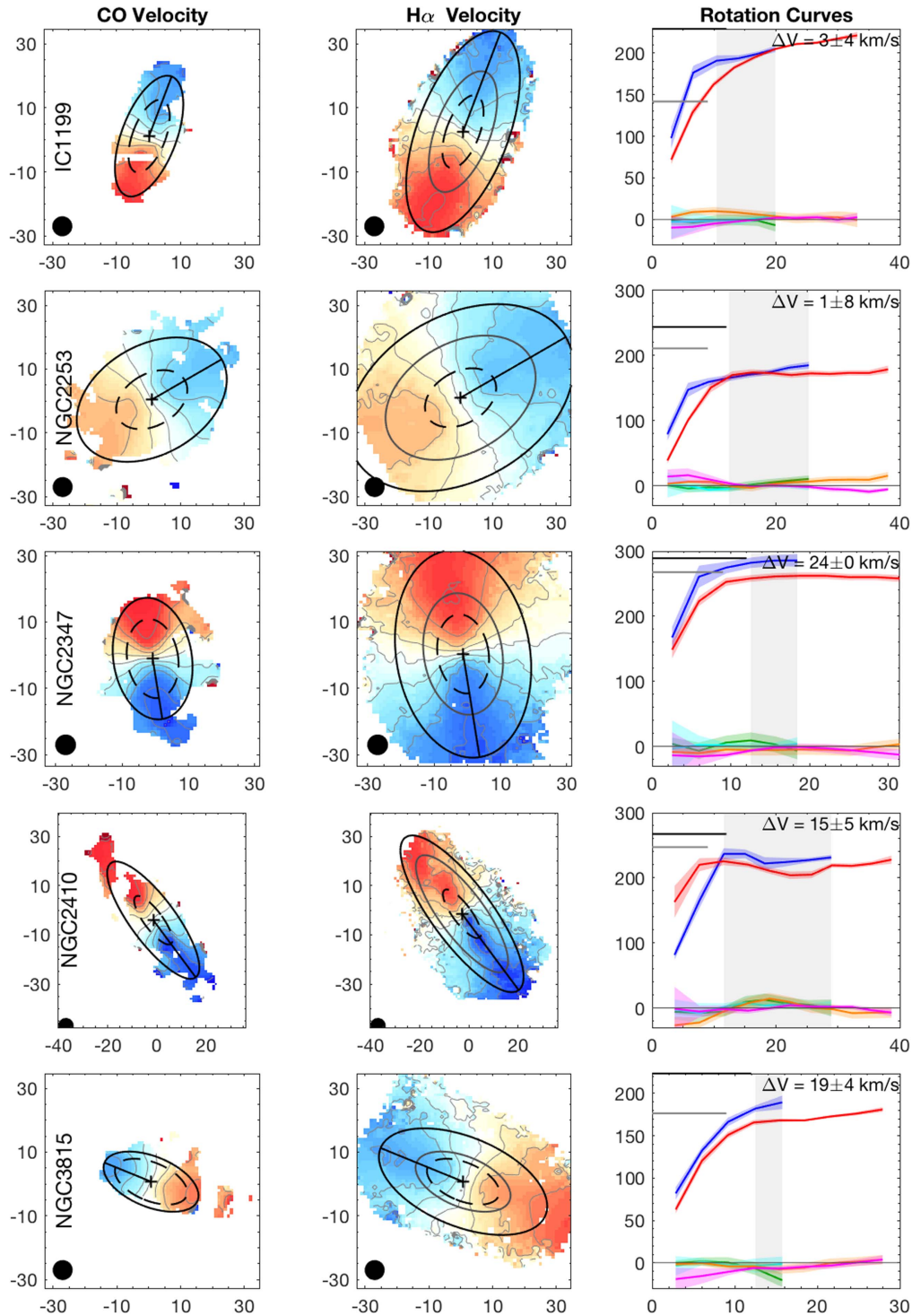
Figure 18. The left column shows the CO velocity fields for the KSS galaxies. The color scale spans ±300 km s^{-1}, with negative velocities showing the approaching side in blue. Isovelocity contours are shown in gray, spanning ±300 in 50 km s^{-1} increments. The values on the x- and y-axes show the offset in arcsec from the center position. The solid black circle shows the 6″ beam size. The cross marks the kinematic center of the galaxy. The black line shows the semimajor axis. The black solid ellipse shows the orientation, and the size corresponds to the outermost ring in the rotation curve. The dashed ellipse indicates twice the CO beam; points within this ellipse are excluded from the rotation curve comparison due to possible beam smearing. The center column shows the Hα velocity fields. The color scale also spans ±300 km s^{-1}. The solid black circle shows the 6″ beam size, the cross marks the kinematic center of the galaxy, and the solid black line shows the semimajor axis. The solid black ellipse shows the orientation, and the size corresponds to the outermost ring in the Hα rotation curve. The gray ellipse shows the outermost CO ring (the same as the black ellipse in the CO velocity panels). The right column shows the CO and Hα rotation curves. The x-axis is galactocentric radius (″) and the y-axis is velocity (km s^{-1}). The colored curves show CO V_{rot} (blue), V_{rad} (green), and V_{sys} (cyan), as well as Hα V_{rot} (red), V_{rad} (orange), and V_{sys} (magenta). The color-shaded regions around the curves show the errors on the rotation curve components from the Monte Carlo analysis. The gray-shaded region shows the radii over which the CO and Hα rotation curves are compared, where the inner radius is twice the CO beam size and the outer radius is the furthest CO extent. The ΔV in the upper right corner is the median difference between the CO and Hα V_{rot} over the gray region, and the error is the standard deviation of the differences at each radius. The thin solid gray line marks $V = 0$. The gray and black horizontal line segments show the H I rotation velocity from W50 and W90, respectively. All H I data have been corrected for inclination, using the values in Table 3.
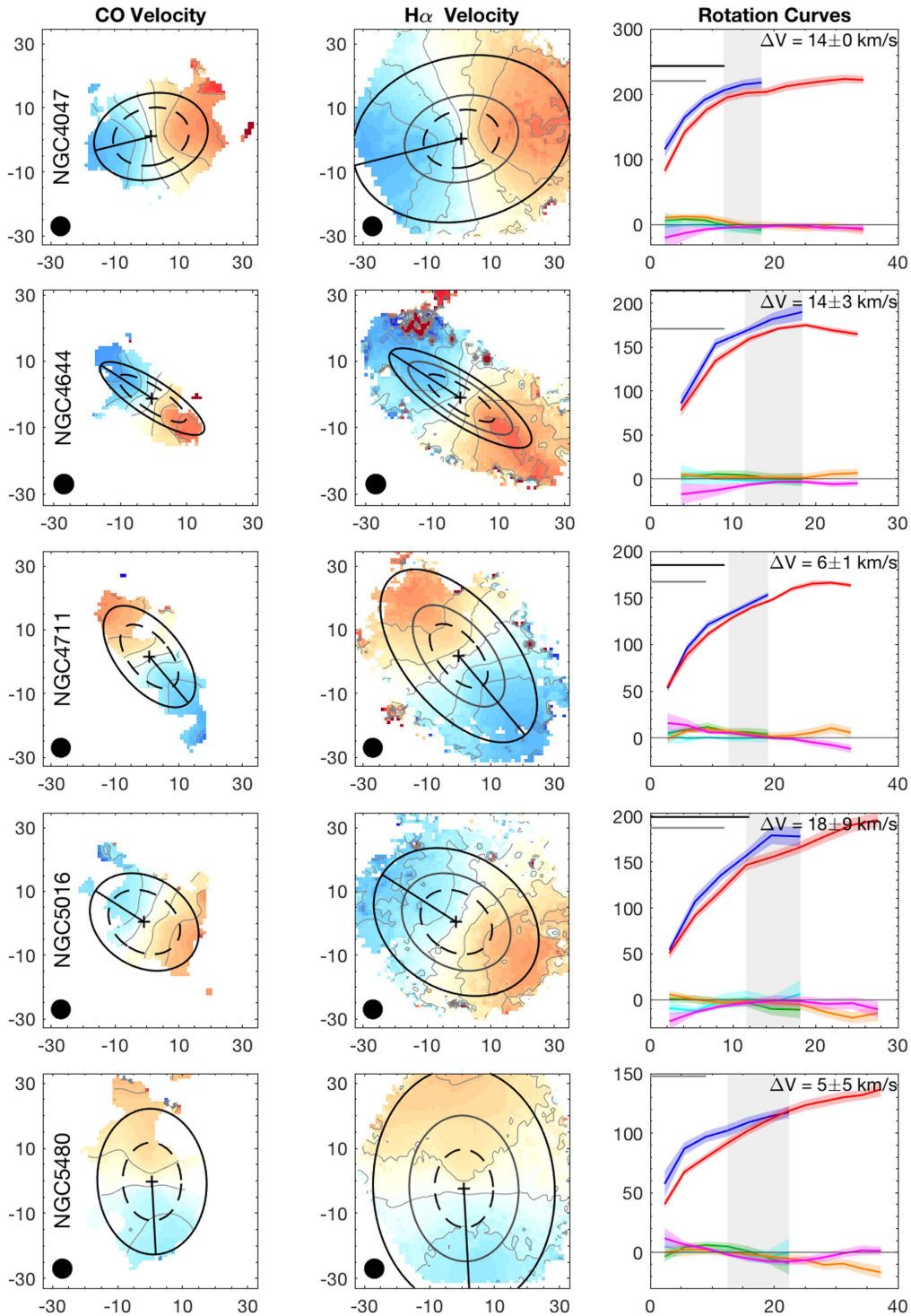
Figure 18. (Continued.)

minimal. This galaxy has a large bulge at redder optical wavelengths, with a B/D ratio of 0.3 in the g-band, 0.7 in the r-band, and 1.1 in the i-band, as well as an average bulge effective radius of 3.5 ± 0.5 kpc (Méndez-Abreu et al. 2017), so bulge contamination is possible.

NGC 2410—Although this galaxy does exhibit non-zero CO and Hα radial and systemic components over the comparison region, the components all track one another, so their effects on ΔV should be minimal. There is a kinematic twist visible in the

Hα velocity field, which is likely responsible for the varying Hα radial component. This feature is less obvious in the CO velocity field. This galaxy has a bar, as listed in Bolatto et al. (2017), which is the likely source of this twist. Both the H I W50 and W90 are higher than the CO $V_{\rm rot}$.

NGC 3815—Although this galaxy has non-zero radial and systemic components over the comparison region, they track each other, so the effect on ΔV should be minimal. The CO and Hα systemic components are near zero. At large radii, the
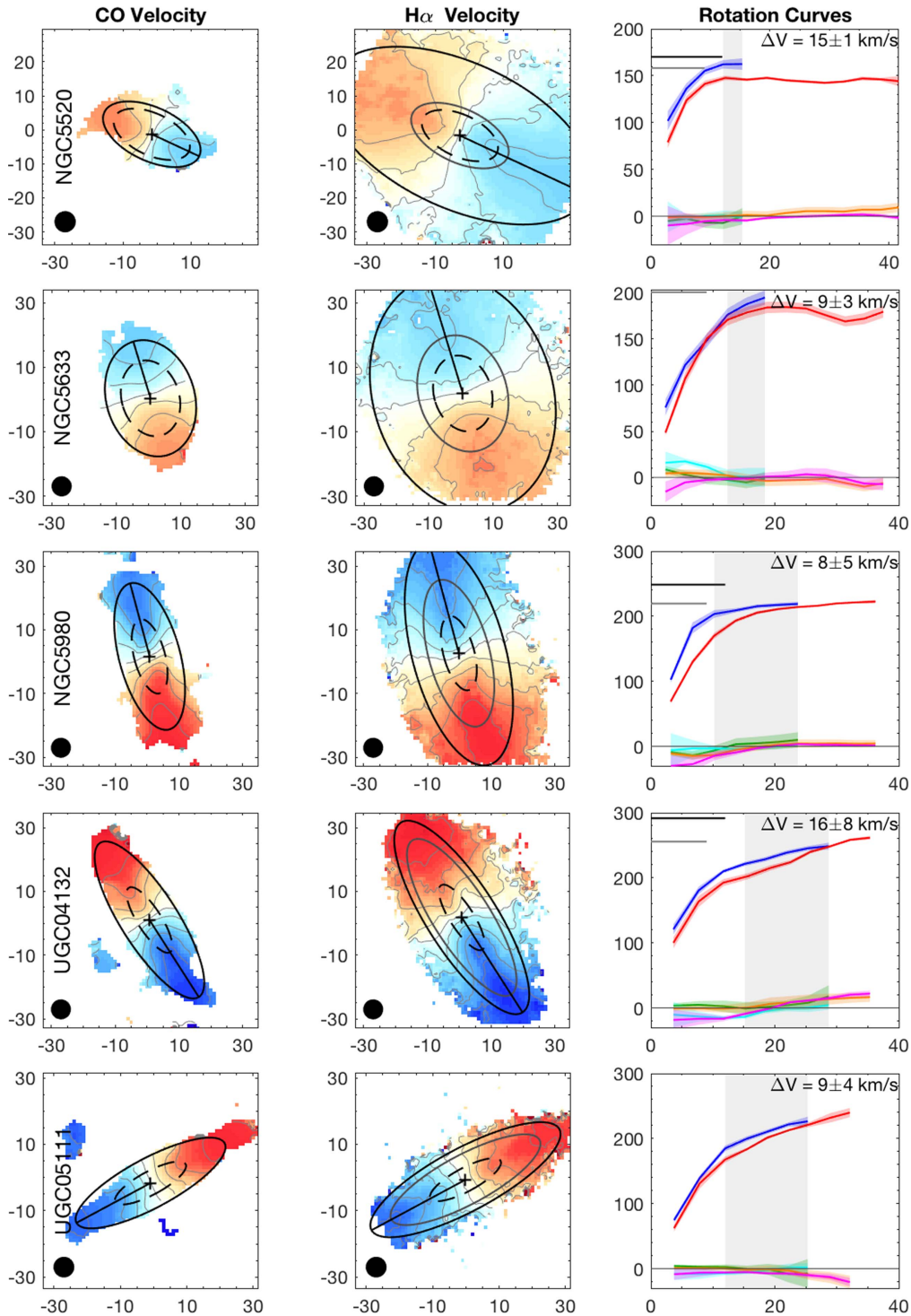
Figure 18. (Continued.)

Hα V_{rot} is consistent with the H I W50, whereas the W90 is much larger than both the CO and Hα V_{rot}.

NGC 4047—This galaxy has excellent CO and Hα rotation curves and velocity fields. At large radii, the H I W50 appears to be consistent with the Hα V_{rot} and potentially the CO V_{rot}. The W90 is much larger.

NGC 4644—This galaxy has excellent CO and Hα rotation curves, with small radial and systemic components overall. Interestingly, this galaxy is listed as having a bar and being a

merger (Bolatto et al. 2017), although there are no obvious signs of either from the velocity fields or rotation curves. The H I W50 tends to agree with the Hα V_{rot}.

NGC 4711—This galaxy has a warp in the center, as seen in the Hα velocity field and rotation component of the rotation curve. It is listed as having a bar (Bolatto et al. 2017), which likely accounts for these features. These are not seen in the CO velocity field or rotation curve. Although both the CO and Hα have non-zero radial components in the comparison region,
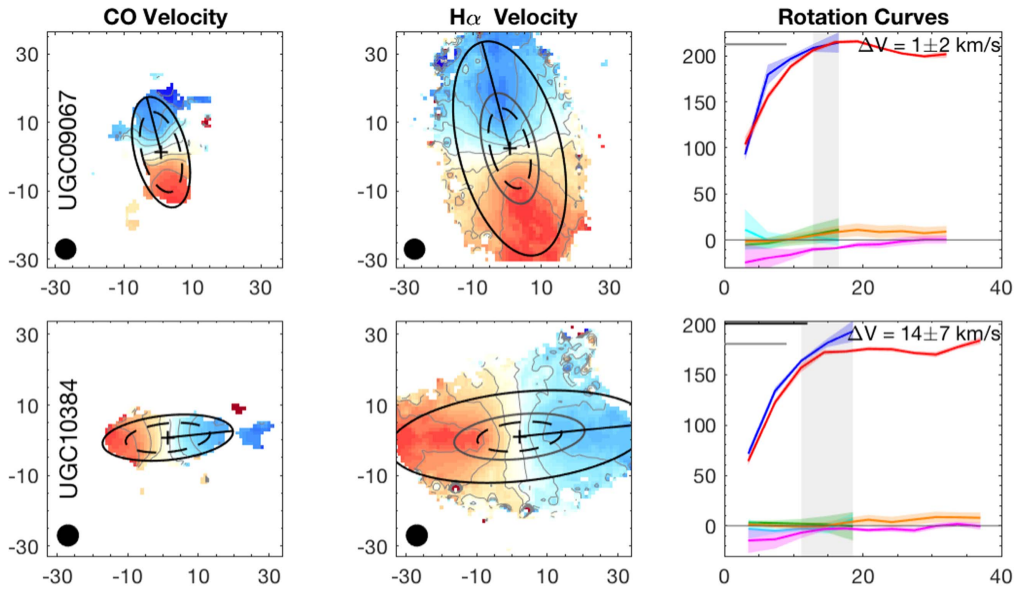
Figure 18. (Continued.)

they track each other closely, so their effect on ΔV is likely small. Neither the CO nor Hα rotation curve flattens over the radii probed, so it is unclear whether the H I W50 or W90 agree with either.

NGC 5016—The $V_{\rm rad}$ and $V_{\rm sys}$ components for CO and Hα are nearly zero over the comparison region, although they deviate at small and large radii. This galaxy has a bar (Bolatto et al. 2017), although it is not obvious from either velocity field. The H I W50 and W90 are more consistent with $V_{\rm rot}$(CO), at least over the comparison region.

NGC 5480—Neither the CO nor Hα rotation curve for this galaxy flattens out to large radii. It has small radial and systemic components over the comparison region, although there is a decreasing trend in the both of these components in Hα. H I data is taken from Springob et al. (2005), using the Green Bank 300 ft telescope.

NGC 5520—The difference between the CO and Hα rotation velocity is striking in this galaxy. The radial and systemic components are all consistent with zero. The Hα rotation curve flattens quickly. The H I data agree well with the CO rotation velocity.

NGC 5633—The CO and Hα rotation velocities are remarkably similar and only begin to deviate in the comparison region. Although there are trends in the radial and systemic components in the center, they are near zero over the radii of interest. This galaxy is known to have a ring structure (Bolatto et al. 2017). H I data is taken from Springob et al. (2005), using the Green Bank 300 ft telescope.

NGC 5980—This galaxy's CO rotation curve flattens, whereas the Hα rotation curve continues to rise slightly. Although the radial and systemic components dip in the center, they are near zero over the radii of interest. There is a kinematic twist visible in both the CO and Hα velocity fields, which likely causes the dip in the radial and systemic components. The H I W50 is close to $V_{\rm rot}$(CO), but the W90 is higher.

UGC 4132—There is an interesting dip in the Hα rotation curve that is not visible in the CO rotation curve. There is also a slight trend in the Hα radial and systemic components. The H I

W50 is close to the CO rotational velocity, but the W90 is substantially larger.

UGC 5111—The CO and Hα velocity fields look different near the major axis; in the Hα velocity fields there are thin regions of high velocities, whereas these larger velocities are not as concentrated along the major axis in the CO velocity field. The radial and systemic components are small over all radii. There are no H I data available for this galaxy from either our GBT observations or from Springob et al. (2005).

UGC 9067—The galaxy's CO and Hα rotation velocities are nearly identical. Both the CO and Hα radial components increase over the comparison region, but have the same values. H I data is taken from Springob et al. (2005), using the Arecibo telescope (line feed system).

UGC 10384—This galaxy has small radial and systemic components over the region of interest, although there are small deviations at small and large radii. The rotation components are identical at small radii, but diverge as the Hα rotation curve flattens while the CO rotation curve continues to rise. The H I W50 and W90 are more consistent with the CO rotation velocity than the Hα.

ORCID iDs

Rebecca C. Levy ⓘ https://orcid.org/0000-0003-2508-2586
Alberto D. Bolatto ⓘ https://orcid.org/0000-0002-5480-5686
Peter Teuben ⓘ https://orcid.org/0000-0003-1774-3436
Sebastián F. Sánchez ⓘ https://orcid.org/0000-0001-6444-9307
Jorge K. Barrera-Ballesteros ⓘ https://orcid.org/0000-0003-2405-7258
Leo Blitz ⓘ https://orcid.org/0000-0002-4272-4432
Rubén García-Benito ⓘ https://orcid.org/0000-0002-7077-308X
Rodrigo Herrera-Camus ⓘ https://orcid.org/0000-0002-2775-0595
Bernd Husemann ⓘ https://orcid.org/0000-0003-2901-6842
Gigi Y. C. Leung ⓘ https://orcid.org/0000-0003-4157-7968

Damián Mast ⓘ https://orcid.org/0000-0003-0469-3193
Dyas Utomo ⓘ https://orcid.org/0000-0003-4161-2639
Glenn van de Ven ⓘ https://orcid.org/0000-0003-4546-7731
Tony Wong ⓘ https://orcid.org/0000-0002-7759-0585

References

Barnabè, M., Ciotti, L., Fraternali, F., & Sancisi, R. 2006, A&A, 446, 61
Barrera-Ballesteros, J. K., Falcón-Barroso, J., García-Lorenzo, B., et al. 2014, A&A, 568, A70
Barrera-Ballesteros, J. K., García-Lorenzo, B., Falcón-Barroso, J., et al. 2015, A&A, 582, A21
Begeman, K. G. 1987, PhD thesis, Kapteyn Institute
Begeman, K. G. 1989, A&A, 223, 47
Binney, J., & Tremaine, S. 2008, Galactic Dynamics (2nd ed.; Princeton, NJ: Princeton Univ. Press)
Blanc, G. A., Heiderman, A., Gebhardt, K., Evans, N. J., II, & Adams, J. 2009, ApJ, 704, 842
Boettcher, E., Gallagher, J. S., III, & Zweibel, E. G. 2017, ApJ, 845, 155
Boettcher, E., Zweibel, E. G., Gallagher, J. S., III, & Benjamin, R. A. 2016, ApJ, 832, 118
Boissier, S., Prantzos, N., Boselli, A., & Gavazzi, G. 2003, MNRAS, 346, 1215
Bolatto, A. D., Wong, T., Utomo, D., et al. 2017, ApJ, 846, 159
Bosma, A. 1978, PhD thesis, Groningen Univ.
Burkert, A., Genzel, R., Bouché, N., et al. 2010, ApJ, 725, 2324
Catalán-Torrecilla, C., Gil de Paz, A., Castillo-Morales, A., et al. 2015, A&A, 584, A87
Chaves, T. A., & Irwin, J. A. 2001, ApJ, 557, 646
Cox, D. P. 1989, in IAU Coll. 120: Structure and Dynamics of the Interstellar Medium 350, Lecture Notes in Physics, ed. G. Tenorio-Tagle, M. Moles, & J. Melnick (Berlin: Springer), 500
Davis, T. A., Alatalo, K., Bureau, M., et al. 2013, MNRAS, 429, 534
de Blok, W. J. G., Walter, F., Brinks, E., et al. 2008, AJ, 136, 2648
de Blok, W. J. G., Walter, F., Smith, J.-D. T., et al. 2016, AJ, 152, 51
Dettmar, R.-J. 1990, A&A, 232, L15
Di Teodoro, E. M., Fraternali, F., & Miller, S. H. 2016, A&A, 594, A77
Falcón-Barroso, J., Lyubenova, M., van de Ven, G., et al. 2017, A&A, 597, A48
Frank, B. S., de Blok, W. J. G., Walter, F., Leroy, A., & Carignan, C. 2016, AJ, 151, 94
Fraternali, F., Oosterloo, T., & Sancisi, R. 2004, A&A, 424, 485
Fraternali, F., Oosterloo, T. A., Sancisi, R., & Swaters, R. 2005, in ASP Conf. Ser. 331, Extra-Planar Gas, ed. R. Braun (San Francisco, CA: ASP), 239
Fraternali, F., van Moorsel, G., Sancisi, R., & Oosterloo, T. 2002, AJ, 123, 3124
García-Benito, R., Zibetti, S., Sánchez, S. F., et al. 2015, A&A, 576, A135
García-Lorenzo, B., Márquez, I., Barrera-Ballesteros, J. K., et al. 2015, A&A, 573, A59
Haffner, L. M., Dettmar, R.-J., Beckman, J. E., et al. 2009, RvMP, 81, 969
Heald, G. H., Rand, R. J., Benjamin, R. A., & Bershady, M. A. 2006a, ApJ, 647, 1018
Heald, G. H., Rand, R. J., Benjamin, R. A., Collins, J. A., & Bland-Hawthorn, J. 2006b, ApJ, 636, 181
Hoopes, C. G., Walterbos, R. A. M., & Rand, R. J. 1999, ApJ, 522, 669
Husemann, B., Jahnke, K., Sánchez, S. F., et al. 2013, A&A, 549, A87
Iorio, G., Fraternali, F., Nipoti, C., et al. 2017, MNRAS, 466, 4159
Jones, G. C., Carilli, C. L., Shao, Y., et al. 2017, ApJ, 850, 180
Kennicutt, R. C., Jr. 1998, ApJ, 498, 541
Krishnarao, D., Haffner, L. M., Benjamin, R. A., Hill, A. S., & Barger, K. A. 2017, ApJ, 838, 43
Kulkarni, S. R., & Heiles, C. 1987, in Astrophysics and Space Science Library 134, Interstellar Processes, ed. D. J. Hollenbach & H. A. Thronson, Jr. (Dordrecht: Reidel), 87
Lacerda, E. A. D., Cid Fernandes, R., Couto, G. S., et al. 2018, MNRAS, 474, 3727

Lee, S.-W., Irwin, J. A., Dettmar, R.-J., et al. 2001, A&A, 377, 759
Leroy, A. K., Walter, F., Brinks, E., et al. 2008, AJ, 136, 2782
Leung, G. Y. C., Leaman, R., van de Ven, G., et al. 2018, MNRAS, 477, 254
Levine, E. S., Heiles, C., & Blitz, L. 2008, ApJ, 679, 1288
López-Cobá, C., Sánchez, S. F., Moiseev, A. V., et al. 2017, MNRAS, 467, 4951
Madsen, G. J. 2004, PhD thesis, The Univ. Wisconsin—Madison, Wisconsin
Madsen, G. J., Reynolds, R. J., & Haffner, L. M. 2006, ApJ, 652, 401
Makarov, D., Prugniel, P., Terekhova, N., Courtois, H., & Vauglin, I. 2014, A&A, 570, A13
Marinacci, F., Fraternali, F., Ciotti, L., & Nipoti, C. 2010, MNRAS, 401, 2451
McKee, C. F. 1990, ASP Conf. Ser. 12, The Evolution of the Interstellar Medium, ed. L. Blitz (San Francisco, CA: ASP), 3
Méndez-Abreu, J., Ruiz-Lara, T., Sánchez-Menguiano, L., et al. 2017, A&A, 598, A32
Mestel, L. 1963, MNRAS, 126, 553
Miller, S. T., & Veilleux, S. 2003a, ApJS, 148, 383
Miller, S. T., & Veilleux, S. 2003b, ApJ, 592, 79
Mogotsi, K. M., de Blok, W. J. G., Caldú-Primo, A., et al. 2016, AJ, 151, 15
Persic, M., & Salucci, P. 1991, ApJ, 368, 60
Persic, M., Salucci, P., & Stel, F. 1996, MNRAS, 281, 27
Rand, R. J. 1996, ApJ, 462, 712
Rand, R. J. 1997, ApJ, 474, 129
Rand, R. J. 2000, ApJL, 537, L13
Rand, R. J., Kulkarni, S. R., & Hester, J. J. 1990, ApJL, 352, L1
Reynolds, R. J. 1971, PhD thesis, The Univ. Wisconsin—Madison
Reynolds, R. J. 1993, in ASP Conf. Ser. 35, Massive Stars: Their Lives in the Interstellar Medium, ed. J. P. Cassinelli & E. B. Churchwell (San Francisco, CA: ASP), 338
Reynolds, R. J., Scherb, F., & Roesler, F. L. 1973, ApJ, 185, 869
Reynolds, R. J., Sterling, N. C., & Haffner, L. M. 2001, ApJL, 558, L101
Rogstad, D. H., Lockhart, I. A., & Wright, M. C. H. 1974, ApJ, 193, 309
Rossa, J., & Dettmar, R.-J. 2003a, A&A, 406, 493
Rossa, J., & Dettmar, R.-J. 2003b, A&A, 406, 505
Sánchez, S. F., García-Benito, R., Zibetti, S., et al. 2016a, A&A, 594, A36
Sánchez, S. F., Kennicutt, R. C., Gil de Paz, A., et al. 2012, A&A, 538, A8
Sánchez, S. F., Pérez, E., Sánchez-Blázquez, P., et al. 2016b, RMxAA, 52, 21
Sánchez, S. F., Pérez, E., Sánchez-Blázquez, P., et al. 2016c, RMxAA, 52, 171
Sánchez, S. F., Rosales-Ortega, F. F., Iglesias-Páramo, J., et al. 2014, A&A, 563, A49
Sanders, D. B., & Mirabel, I. F. 1996, ARA&A, 34, 749
Sault, R. J., Teuben, P. J., & Wright, M. C. H. 1995, in ASP Conf. Ser. 77, Astronomical Data Analysis Software and Systems IV, ed. R. A. Shaw, H. E. Payne, & J. J. E. Hayes (San Francisco, CA: ASP), 433
Schaap, W. E., Sancisi, R., & Swaters, R. A. 2000, A&A, 356, L49
Schoenmakers, R. H. M. 1999, PhD thesis, Univ. Groningen
Simon, J. D., Bolatto, A. D., Leroy, A., Blitz, L., & Gates, E. L. 2005, ApJ, 621, 757
Spitzer, L., Jr. 1942, ApJ, 95, 329
Springob, C. M., Haynes, M. P., Giovanelli, R., & Kent, B. R. 2005, ApJS, 160, 149
Swaters, R. A. 1999, PhD thesis, Rijksuniversiteit Groningen
Swaters, R. A., Sancisi, R., & van der Hulst, J. M. 1997, ApJ, 491, 140
Teuben, P. 1995, in ASP Conf. Ser. 77, Astronomical Data Analysis Software and Systems IV, ed. R. A. Shaw, H. E. Payne, & J. J. E. Hayes (San Francisco, CA: ASP), 398
Utomo, D., Bolatto, A. D., Wong, T., et al. 2017, ApJ, 849, 26
van de Ven, G., & Fathi, K. 2010, ApJ, 723, 767
van der Kruit, P. C. 1988, A&A, 192, 117
Vargas, C. J., Heald, G., Walterbos, R. A. M., et al. 2017, ApJ, 839, 118
Walcher, C. J., Wisotzki, L., Bekeraité, S., et al. 2014, A&A, 569, A1
Wong, T., Blitz, L., & Bosma, A. 2004, ApJ, 605, 183
Yim, K., Wong, T., Xue, R., et al. 2014, AJ, 148, 127
Zschaechner, L. K., & Rand, R. J. 2015, ApJ, 808, 153
Zschaechner, L. K., Rand, R. J., & Walterbos, R. 2015, ApJ, 799, 61